



# AMERICAN METEOROLOGICAL SOCIETY

*Journal of Climate*

## **EARLY ONLINE RELEASE**

This is a preliminary PDF of the author-produced manuscript that has been peer-reviewed and accepted for publication. Since it is being posted so soon after acceptance, it has not yet been copyedited, formatted, or processed by AMS Publications. This preliminary version of the manuscript may be downloaded, distributed, and cited, but please be aware that there will be visual differences and possibly some content differences between this version and the final published version.

The DOI for this manuscript is doi: 10.1175/JCLI-D-17-0586.1

The final published version of this manuscript will replace the preliminary version at the above DOI once it is available.

If you would like to cite this EOR in a separate work, please use the following full citation:

Hill, P., R. Allan, J. Chiu, A. Bodas-Salcedo, and P. Knippertz, 2018: Quantifying the contribution of different cloud types to the radiation budget in southern West Africa. *J. Climate*. doi:10.1175/JCLI-D-17-0586.1, in press.

© 2018 American Meteorological Society



1 **Quantifying the contribution of different cloud types to the radiation budget**  
2 **in southern West Africa**

3 Peter G. Hill\*

4 *University of Reading, Reading, UK*

5 Richard P. Allan

6 *University of Reading, Reading, UK; National Centre for Earth Observation, Reading, UK*

7 J. Christine Chiu

8 *University of Reading, Reading, UK; Colorado State University, Fort Collins, USA*

9 Alejandro Bodas-Salcedo

10 *Met Office Hadley Centre, Exeter, UK*

11 Peter Knippertz

12 *Institute of Meteorology and Climate Research, Karlsruhe Institute of Technology, Karlsruhe,*  
13 *Germany*

14 \*Corresponding author address: Department of Meteorology, University of Reading, Reading, UK

15 E-mail: p.g.hill@reading.ac.uk

## ABSTRACT

16 The contribution of cloud to the radiation budget of southern West Africa  
17 (SWA) is poorly understood yet is important for understanding regional mon-  
18 soon evolution and for evaluating and improving climate models, which have  
19 large biases in this region. Radiative transfer calculations applied to at-  
20 mospheric profiles obtained from the CERES-CloudSat-CALIPSO-MODIS  
21 (CCCM) dataset are used to investigate the effects of 12 different cloud types  
22 (defined by their vertical structure) on the regional energy budget of SWA (5–  
23 10 °N, 8 °W–8 °E) during June–September. We show that the large regional  
24 mean cloud radiative effect in SWA is due to non-negligible contributions  
25 from many different cloud types; 8 cloud types have a cloud fraction larger  
26 than 5 % and contribute at least 5 % of the regional mean shortwave cloud  
27 radiative effect at the top of atmosphere. Low-clouds, which are poorly ob-  
28 served by passive satellite measurements, were found to cause net radiative  
29 cooling of the atmosphere, which reduces the heating from other cloud types  
30 by approximately 10 %. The sensitivity of the radiation budget to underes-  
31 timating low-cloud cover is also investigated. The radiative effect of miss-  
32 ing low-cloud is found to be up to approximately  $-25 \text{ W m}^{-2}$  for upwelling  
33 shortwave irradiance at the top of atmosphere and  $35 \text{ W m}^{-2}$  for downwelling  
34 shortwave irradiance at the surface.

## 35 **1. Introduction**

36 The West African Monsoon (WAM) is an important climatological system globally that plays a  
37 key role in the climate of sub-Saharan West Africa where many countries rely on the WAM for  
38 most of their rainfall (e.g., Nicholson and Grist 2003). Despite its importance, WAM precipitation  
39 is not well represented in climate models, which are unable to reproduce the observed intermit-  
40 tence and intraseasonal variability of precipitation in West Africa (Roehrig et al. 2013). Moreover,  
41 large differences exist between the accumulated WAM precipitation simulated by different mod-  
42 els (Hourdin et al. 2010). These errors lead to a large spread and low confidence in projections  
43 of future precipitation in West Africa in climate models (e.g., Cook and Vizy 2006; Paeth et al.  
44 2011).

45 WAM precipitation is difficult to model because it depends on a number of complex factors,  
46 including, but not limited to, the regional energy budget. Numerous modeling studies have shown  
47 the sensitivity of the WAM circulation to changes in the modeled shortwave (SW) and longwave  
48 (LW) radiation. Tompkins (2005) and Rodwell and Jung (2008) showed circulation and precipi-  
49 tation differences over West Africa arising from the direct radiative effect of aerosol climatology  
50 changes in the European Centre for Medium-Range Weather Forecasts (ECMWF) model. The  
51 strength of the WAM in the Met Office Unified Model (UM) is also affected by changes to clouds  
52 and hence radiation (Marsham et al. 2013; Birch et al. 2014). More recently, Li et al. (2015) high-  
53 lighted a strong sensitivity of the WAM circulation and associated precipitation to the radiation  
54 schemes used in their simulations.

55 Given this sensitivity of the WAM circulation and precipitation to radiation budget changes, it  
56 is important to ensure that simulated radiative properties in models are realistic. Unfortunately,  
57 climate models have large cloud and hence radiation errors in this region (Roehrig et al. 2013).

58 These model errors are persistent in higher resolution simulations (Stein et al. 2015), and partic-  
59 ularly large in southern West Africa (SWA) during the summer (Hannak et al. 2017). Reducing  
60 these model errors requires an improved understanding of how clouds affect the radiation budget  
61 of West Africa, but the complex cloud climatology with frequent multilayer clouds in this region  
62 (Stein et al. 2011) makes it difficult to identify cloud types and to attribute model errors to differ-  
63 ent cloud regimes. A lack of surface-based cloud observations (e.g., Knippertz et al. 2015b) and  
64 uncertain aerosol-cloud interactions (e.g., Knippertz et al. 2015a) further limit understanding of  
65 clouds in this region.

66 The main objective of this article is to quantify the occurrence and radiative effects of differ-  
67 ent cloud types in the SWA region during the monsoon season. Previous studies have quantified  
68 cloud radiative effects for different cloud types on global scales (e.g., Hartmann et al. 1992; Futyan  
69 et al. 2005; Oreopoulos et al. 2017). In West Africa, detailed analyses of cloud radiative effects  
70 have been limited to a single location (Niamey) north of SWA (Bouniol et al. 2012; Miller et al.  
71 2012; Collow et al. 2015). Consequently, the radiative effects of different cloud types have yet to  
72 be quantified and remain highly uncertain in SWA. Low-clouds are prevalent in SWA during the  
73 summer (e.g., Schrage et al. 2006; Schuster et al. 2013; van der Linden et al. 2015; Adler et al.  
74 2017) but poorly represented in climate models (Knippertz et al. 2011). Low-clouds are also dif-  
75 ficult to observe with satellites as they are often obscured by higher clouds (van der Linden et al.  
76 2015; Hill et al. 2016) and as a result remain poorly understood in this region. Consequently, we  
77 place a particular emphasis on low-clouds in this study. To capitalize on the profiling capabil-  
78 ity of active remote sensing, we use the CERES-CloudSat-CALIPSO-MODIS (CCCM) dataset  
79 (Kato et al. 2010, 2011; Ham et al. 2017), which combines observations from active and passive  
80 instruments. Using CCCM data as input to radiative transfer calculations, we can investigate ra-

81 diative effects of different cloud types at TOA, at the surface, and on heating and cooling in the  
82 atmosphere.

## 83 **2. Methods**

### 84 *a. CCCM dataset and radiative transfer calculations*

85 In this study, we calculate and analyze cloud radiative effects for June—September in the region  
86 bounded by 8 °W, 8 °E, 5 °N, and 10 °N. This time period and region was chosen to coincide  
87 with previous and ongoing research within the Dynamics-Aerosol-Chemistry-Cloud Interactions  
88 in West Africa (DACCIWA) project (e.g., Knippertz et al. 2015b; Hill et al. 2016; Hannak et al.  
89 2017). Moreover, this domain strikes a balance between being sufficiently large to minimize  
90 statistical sampling errors and being sufficiently homogeneous for domain mean values to remain  
91 meaningful. We use release B1 of the CCCM dataset (Kato et al. 2010, 2011), which is available  
92 from July 2006—April 2011 inclusive. As this study focuses on the monsoon season (defined  
93 as June—September) over SWA, the resulting data length is 19 months. The satellites used to  
94 generate the CCCM product are polar orbiting, crossing the equator at approximately 1.30 a.m.  
95 and p.m. local time.

96 The CCCM dataset contains those CERES and MODIS footprints that correspond to the  
97 CloudSat-CALIPSO ground track (Fig. 1). CERES (Clouds and the Earth’s Radiant Energy Sys-  
98 tem) and MODIS (Moderate Resolution Imaging Spectroradiometer) are passive instruments pro-  
99 viding information on the radiative properties at the TOA, while the CloudSat radar and CALIPSO  
100 (Cloud-Aerosol Lidar and Infrared Pathfinder Satellite) lidar are active instruments that provide  
101 detailed vertical structure. The CERES optical footprint is 20 km; adding the time response results

102 in a point-spread function of approximately 35 km. Consequently, each CERES footprint contains  
103 approximately 30 CloudSat profiles and 100 CALIPSO profiles.

104 To reduce data volumes, the CloudSat-CALIPSO profiles within each footprint are grouped  
105 based on their vertical structure. First CloudSat and CALIPSO observations are merged on to  
106 a common 1x1 km horizontal grid. Within each profile, cloud top and base height for up to  
107 6 cloud layers are estimated from the CloudSat cloud classification product and the CALIPSO  
108 vertical feature mask. Profiles with the same cloud top and base height are combined to form  
109 up to 16 cloud groups. For further details on the grouping process, see Kato et al. (2010). For  
110 each cloud group, cloud properties are derived from a combination of CloudSat, CALIPSO and  
111 MODIS measurements, as described by Bodas-Salcedo et al. (2016), with a vertical resolution of  
112 approximately 240 m. For simplicity, we shall refer to these groups as ‘CCCM group profiles’  
113 hereafter.

114 The CCCM dataset is used as input to radiative transfer calculations using the SOCRATES  
115 (Suite Of Community RAdiative Transfer codes based on Edwards and Slingo) two-stream ra-  
116 diation scheme (Edwards and Slingo 1996) to obtain radiative fluxes and heating rates for each  
117 profile. The CCCM group profiles provide cloud water content and liquid droplet effective ra-  
118 dius. Temperature, water vapor, surface and aerosol properties are also obtained from the CCCM  
119 dataset, as described below, but do not vary within CERES footprints. The CCCM dataset includes  
120 calculated profiles of irradiances and heating rates for each CERES footprint; our new calculations  
121 are necessary to provide irradiances and heating rates for the individual cloud groups within each  
122 CERES footprint, which are not available in the CCCM product.

123 The treatment of cloud in our radiative transfer calculations follows Bodas-Salcedo et al. (2016),  
124 except for two changes. First, we changed the cloud phase when the combination of cloud tem-  
125 perature (based on Goddard Earth Observing System Model (GEOS) reanalyses) and cloud phase

126 (based on the CloudSat phase) reported by CCCM was unphysical (i.e., water cloud at tempera-  
127 tures below 233 K and ice cloud at temperatures above 273 K). Our second change relates to the  
128 parametrization used within the radiative transfer model to calculate the single scattering proper-  
129 ties of clouds from the cloud bulk microphysical properties. We use a different parameterization of  
130 ice single scattering properties (Baran et al. 2013), because it results in better agreement between  
131 our calculations and the CERES measurements at the TOA. Our radiative transfer calculations  
132 were quite sensitive to the choice of parametrization of ice single scattering properties. For exam-  
133 ple, using a different parametrization of ice single scattering properties (Baran et al. 2016) in our  
134 calculations increases the mean TOA cloud radiative effects for all high cloud types, by 27 – 78  
135  $\text{W m}^{-2}$  in the SW and by 5 – 21  $\text{W m}^{-2}$  in the LW.

136 The CCCM dataset provides a profile of aerosol type and mean aerosol extinction for each  
137 CERES footprint. Seven common aerosol species are represented, including soluble and insoluble  
138 particles, small and large dust particles, sulfuric acid, sea salt, and soot. The spectrally varying  
139 extinction, single scattering albedo, and asymmetry of these aerosol species are parameterized  
140 in the SOCRATES code as a function of aerosol mass mixing ratio, as described in Cusack et al.  
141 (1998). For each aerosol type, we use the inverse of the SOCRATES parameterization of extinction  
142 to derive profiles of aerosol mass mixing ratios from the aerosol extinction profiles. These aerosol  
143 mass mixing profiles are used as input to the SOCRATES calculations, ensuring that the aerosol  
144 extinction profiles in our calculations and the CCCM dataset match.

145 Our radiative transfer calculations require knowledge of surface albedo in the SW spectral region  
146 and surface emissivity in the LW region. When available, we take MODIS narrowband surface  
147 albedo measurements from the CCCM product, which are converted to average albedo values for  
148 the SOCRATES spectral bands through linear interpolation with weighting by the solar spectrum.  
149 When the MODIS surface spectral albedo is not available, the broadband surface albedo from

150 CERES is applied over land, and a broadband surface albedo as a function of solar zenith angle  
151 (Taylor et al. 1996) is applied over ocean. In the LW spectral region, the surface emissivity from  
152 CERES products is applied for all cases.

### 153 *b. Validation of calculations*

154 To evaluate the reliability of these calculations, we perform a point-to-point comparison be-  
155 tween calculated irradiances at the TOA and coincident CERES observations, as shown in Fig. 2.  
156 SOCRATES irradiances corresponding to different CCCM groups are weighted by the fraction of  
157 the corresponding CERES footprint they occupy. Due to differences in swath and pixels sizes be-  
158 tween the different instruments (e.g. Fig. 1), the CCCM group profiles used for our radiative trans-  
159 fer calculations correspond to a narrow swath within the coincident CERES footprint, rather than  
160 the entire footprint. This representativeness difference may lead to non-negligible discrepancies  
161 between calculated and CERES-observed irradiances. However, we expect these discrepancies to  
162 be random, rather than systematic; therefore, this intercomparison provides a fair evaluation of our  
163 calculations. In general, the calculations show good agreement with the CERES measurements.  
164 The calculated OSR has a bias of  $-4.65 \text{ W m}^{-2}$  and a Pearson correlation coefficient of 0.92 with  
165 the CERES observations. For the outgoing LW radiative fluxes (OLR) there are notable day-night  
166 differences: at night the bias is  $-1.13 \text{ W m}^{-2}$  and the correlation is 0.91, while during the day the  
167 bias is larger ( $-20.50 \text{ W m}^{-2}$ ) and the correlation is smaller (0.85). The large daytime bias in OLR  
168 is evident in Fig. 2b, as a significant proportion of the calculated irradiances are much lower than  
169 the coincident CERES observations.

170 The potential causes of the large bias in the calculated daytime OLR include the input CCCM  
171 group profiles and the approximations made in the SOCRATES scheme. The representativeness  
172 difference, highlighted above, is not expected to cause systematic differences between the cal-

173 culations and the CERES observations. For each CERES footprint, the CCCM dataset includes  
174 radiative fluxes computed using various different treatments of clouds and aerosol. Interestingly,  
175 the CCCM irradiance calculations suffer from a similar magnitude daytime OLR bias in the DAC-  
176 CIWA region (Ham et al. 2017). The large bias also persists when we re-ran SOCRATES with the  
177 temperature-dependent parameterization of ice optical properties described by Baran et al. (2016).  
178 These findings help rule out the possibility that the OLR bias is due to the radiative transfer models  
179 themselves.

180 Cloud extinction within each CCCM group profile is normalized so that the total cloud optical  
181 depth matches that retrieved from MODIS. As different algorithms are used to retrieve cloud op-  
182 tical depth from MODIS measurements during the day and at night (Minnis et al. 2011), differing  
183 biases between day and night may be expected. However, one would expect the MODIS optical  
184 depth retrieval to be more reliable during the day when the SW measurements provide additional  
185 information. The OSR bias is relatively small, which suggests that the daytime total cloud optical  
186 depth is reasonable. Consequently, the error in the CCCM group profiles is most likely in the  
187 vertical distribution of cloud extinction, which has a large effect on the OLR but little effect on  
188 OSR.

189 One possible bias in the input CCCM group profile is the misattribution of low-cloud extinc-  
190 tion detected by MODIS to higher altitude cloud in the CCCM dataset, due to undetected low-  
191 cloud layers. The combined active measurements from CALIPSO and CloudSat provide the best  
192 satellite-based estimate of low-cloud, but detection of low-cloud remains challenging in some sce-  
193 narios. For example, CloudSat is unable to detect all boundary layer clouds due to ground clutter,  
194 and CALIPSO is unable to detect lower clouds when high clouds with optical depth greater than 2  
195 – 3 exist and completely attenuate the lidar signal (Mace et al. 2009). Low-cloud is more common  
196 during the day as discussed in section 3, so this problem is likely to be more significant during

197 the day. If low-cloud is missing in the CloudSat and CALIPSO profiles, then the normalization of  
198 optical depth by MODIS may lead to an attribution of low-cloud extinction to higher-level clouds.  
199 This would lead to a reduction in OLR, while having little impact on the OSR, which is consistent  
200 with the daytime SOCRATES calculations. We shall refer to this as the “low-cloud misattribution”  
201 hypothesis throughout this article.

### 202 *c. Diurnal mean approximation*

203 Surface based synoptic and geostationary satellite observations show maximum low-cloud oc-  
204 currence in SWA at approximately 1000 UTC and minimum at 1800 UTC (van der Linden et al.  
205 2015). Moreover, like much of the tropics, SWA has a diurnal cycle in high cloud linked to the  
206 occurrence of convection, with more high cloud at night than during the day (e.g. Hill et al. 2016).  
207 As the CCCM product is based on polar orbiting satellite measurements, it overpasses SWA at  
208 only two points in the diurnal cycle and clearly will not capture this complex cloud diurnal vari-  
209 ability. However, estimates of the diurnal mean irradiances are required to analyze the contribution  
210 of different cloud types to the mean radiation budget.

211 We use different methods to approximate the diurnal mean radiative effect of different cloud  
212 types in the SW and LW regions. For a SW diurnal mean approximation, we conducted further  
213 calculations with solar zenith angles corresponding to each hour of the diurnal cycle. The hourly  
214 calculations based on 13:30 profiles were averaged together to approximate the diurnal mean, as  
215 we assume 13:30 cloud properties are more representative of mean daylight conditions than 01:30  
216 cloud properties. The hourly calculations based on 01:30 profiles are averaged together to obtain  
217 a second estimate, which we use to derive the uncertainty due to diurnal changes in cloud, as  
218 described in section 2e. For a LW diurnal mean approximation, we simply average the mean

219 irradiances at 13:30 and 01:30, which is consistent with several previous studies (e.g., Hong et al.  
220 2016).

221 To evaluate our diurnal mean approximations, we compare our results to Geostationary Earth  
222 Radiation Budget (GERB) measurements of TOA irradiances (Harries et al. 2005; Dewitte et al.  
223 2008) for the same time period and region as CCCM. With a temporal resolution of 15 minutes  
224 the GERB HR (high-resolution) measurements resolve the diurnal cycle of TOA irradiances. The  
225 GERB product does not report SW outgoing radiative fluxes (OSR) for solar zenith angles larger  
226 than  $80^\circ$ . For zenith angles between  $86.5^\circ$  and  $104.5^\circ$ , we use mean twilight values from CERES  
227 (Kato 2003). For zenith angles between  $80.0^\circ$  and  $86.5^\circ$ , where CERES twilight values are not  
228 reported, we use linear interpolation in time between the GERB measurements and the CERES  
229 twilight values.

230 For OSR, GERB has a regional diurnal mean of  $149 \text{ W m}^{-2}$ . Applying our SW diurnal mean  
231 approximation to our SOCRATES calculations results in a regional mean OSR of  $144 \text{ W m}^{-2}$  when  
232 we use the 13:30 CCCM data, and  $125 \text{ W m}^{-2}$  when we use the 01:30 CCCM data. Estimating the  
233 OSR using the LW diurnal mean approximation (i.e. by averaging the mean OSR at 13:30 ( $376$   
234  $\text{ W m}^{-2}$ ) and the mean OSR at 01:30 ( $0 \text{ W m}^{-2}$ )) gives an OSR of  $188 \text{ W m}^{-2}$ . For OLR, GERB has  
235 a regional mean of  $230 \text{ W m}^{-2}$ . Applying our LW diurnal mean approximation to our SOCRATES  
236 calculations results in a regional mean of  $220 \text{ W m}^{-2}$ . We can separate the calculation bias and  
237 the LW diurnal mean approximation bias by applying our LW diurnal mean approximation to the  
238 CERES OLR measurements in the CCCM product, as these measurements represent the OLR we  
239 would obtain if the calculations were unbiased. Applying the LW diurnal mean approximation to  
240 the CERES measurements results in the same value as averaging the GERB diurnal mean:  $230$   
241  $\text{ W m}^{-2}$ . This shows that the bias in the LW diurnal mean approximation when applied to our LW  
242 calculations is due to the bias in the calculated OLR at 13:30.

243 *d. Definition of cloud types and cloud radiative effects*

244 Based on the classification scheme described in Tselioudis et al. (2013), we assign a cloud type  
245 to each CCCM group profile, based on cloud vertical structure. Pressure thresholds of 680 and 440  
246 hPa are used to classify each CCCM group profile according to whether it contains one or more of  
247 low- (L), mid- (M), or high-level (H) cloud and whether cloud in different layers is connected or  
248 not. As illustrated in Fig. 3, this classification results in 13 different scene types: clear-sky and 12  
249 cloud types. Cloud occurring in multiple layers is denoted by a letter for each layer it occurs in,  
250 while ‘x’ is used to denote when cloud extends across the pressure boundaries. For convenience,  
251 we use *isolated low-cloud* to refer to CCCM group profiles that contain only low-cloud (i.e. 1L),  
252 *discontiguous low-cloud* to low-cloud that occurs beneath distinct higher clouds (i.e. ML, HL,  
253 HxML, and HML), and *contiguous low-cloud* to scenes where the cloud extends vertically from  
254 the low layer to higher layers (i.e. MxL, HMxL, HxMxL). Note that passive sensors can only  
255 identify isolated low-clouds, since high clouds in the other two categories will obscure low-clouds.

256 In this article we calculate the cloud radiative effect (*CRE*) by

$$CRE = (I_{\downarrow}^{all} - I_{\uparrow}^{all}) - (I_{\downarrow}^{clr} - I_{\uparrow}^{clr}) \quad (1)$$

257 where  $I^{all}$  denotes the all-sky irradiance calculated by SOCRATES,  $I^{clr}$  is the clear-sky irradiance,  
258 calculated by repeating the SOCRATES calculations without cloud,  $I_{\downarrow}$  denotes a downwelling  
259 irradiance and  $I_{\uparrow}$  denotes an upwelling irradiance. This method is applied to calculate both TOA  
260 and surface *CRE*s; in-atmosphere *CRE*s are calculated by subtracting the surface *CRE* from the  
261 TOA *CRE*.

262 Let  $f_{i,j}$  be the fraction of the  $i$ -th CERES footprint occupied by the  $j$ -th CCCM group profile,  
263 and  $CRE_{i,j}$  be the corresponding *CRE* (See Fig. 3). Then the regional mean *CRE* can be calculated

264 by

$$CRE = \frac{\sum_i \left[ \sum_{j=1}^{n_i} f_{i,j} \cdot CRE_{i,j} \right]}{\sum_i \left[ \sum_{j=1}^{n_i} f_{i,j} \right]} \quad (2)$$

265 where  $n_i$  is the number of CCCM group profiles (at most 16) in the  $i$ -th CERES footprint.

266 After classification, each CCCM group profile corresponds to one of 13 scene types. The con-  
267 tribution from each scene type to the regional mean  $CRE$  ( $CRE^k$ ) can be calculated by

$$CRE^k = \frac{\sum_i \left[ \sum_{j=1}^{n_i} \delta_{t(i,j)k} \cdot f_{i,j} \cdot CRE_{i,j} \right]}{\sum_i \left[ \sum_{j=1}^{n_i} f_{i,j} \right]} \quad (3)$$

268 where  $t(i, j)$  is the scene type of the  $j$ -th CCCM group profile in the  $i$ -th CERES footprint and  
269  $\delta_{t(i,j)k}$  is the Kronecker delta function, which equals one if  $t(i, j) = k$  and zero otherwise. This  
270  $\delta_{t(i,j)k}$  term ensures that only scenes of type  $k$  are included in the contribution of scene type  $k$  to  
271 the regional mean  $CRE$ .

272 Using these 13 scene types, since each CCCM group profile is assigned to a single scene type,  
273 we can rewrite the  $CRE$  as

$$CRE = \sum_{k=1}^{13} CRE^k \quad (4)$$

274 Since the  $CRE$  for the clear-sky scene is zero, in practice we only need to sum over the 12 cloud  
275 types.

276 To provide further insight into how different cloud types affect the regional energy budget, the  
277 contribution to the total cloud radiative effect from each cloud type ( $CRE^k$ , eq. 3) can be fur-  
278 ther decomposed into its frequency of occurrence ( $F^k$ ) and mean coincident cloud radiative effect  
279 ( $CCRE^k$ : the mean radiative effect calculated using only the CCCM group profiles that correspond  
280 to that cloud type).  $F^k$  is calculated by summing the fraction of each CERES footprint assigned to  
281 that cloud type  $k$  and dividing by the total number of CERES footprints:

$$F^k = \frac{\sum_i \left[ \sum_{j=1}^{n_i} \delta_{t(i,j)k} \cdot f_{i,j} \right]}{\sum_i \left[ \sum_{j=1}^{n_i} f_{i,j} \right]}, \quad (5)$$

282  $CCRE^k$  is calculated by averaging the  $CRE$ s for all the CCCM group profiles assigned to cloud  
 283 type  $k$ , weighted by the fraction of a CERES footprint assigned to each CCCM group profile:

$$CCRE^k = \frac{\sum_i \left[ \sum_{j=1}^{n_i} \delta_{t(i,j)k} \cdot f_{i,j} \cdot CRE_{i,j} \right]}{\sum_i \left[ \sum_{j=1}^{n_i} \delta_{t(i,j)k} \cdot f_{i,j} \right]}. \quad (6)$$

284 Then the contribution from each cloud type to the regional mean cloud radiative effect ( $CRE^k$ ) can  
 285 be calculated by

$$CRE^k = F^k CCRE^k. \quad (7)$$

286 This decomposition can also reveal hidden biases in atmospheric models, where compensating er-  
 287 rors in cloud frequency of occurrence and cloud radiative properties can lead to reasonable regional  
 288 mean irradiances (e.g. Nam et al. 2012).

### 289 *e. Treatment of uncertainty in cloud radiative effects*

290 We account for three distinct sources of uncertainty in the  $CRE$ s calculated in this article: sam-  
 291 pling, the diurnal approximations, and the radiative transfer calculations. We estimate the uncer-  
 292 tainty from each of these sources independently and then derive the total uncertainty by combining  
 293 them in quadrature.

294 We perform radiative transfer calculations for a large number of CERES footprints (approx-  
 295 imately 9,600 daytime and 9,100 nighttime). However, as we are not continuously sampling the  
 296 entire domain, any quantity we derive from these calculations will be subject to a statistical sam-  
 297 pling error. We estimate sampling errors by bootstrap sampling of the CERES footprints. The  
 298 bootstrapping is performed separately for day and night, and 200 bootstrap samples are used. Un-  
 299 certainty for each cloud type is then calculated as the standard deviation of the mean  $CRE^k$  in  
 300 each of the bootstrap samples. The magnitude of this uncertainty is quite small; for each of the

301 contributions of the different cloud types to the regional mean *CRE*, it is less than  $1.5 \text{ W m}^{-2}$  for  
302 both SW and LW.

303 Given that they are based on only two points in the diurnal cycle, our approximations for the  
304 diurnal mean irradiance represent an additional source of uncertainty. The SW diurnal approxi-  
305 mation uncertainty is estimated by the absolute value of the difference between the SW diurnal  
306 mean approximation (i.e. based on calculations using the 13:30 CCCM data) and the SW diurnal  
307 mean calculations using the 01:30 CCCM data. In the LW, the diurnal approximation uncertainty  
308 is estimated by the difference between the LW diurnal mean approximation and the LW calcu-  
309 lations at either 13:30 or 01:30 (since the LW diurnal mean is approximated by the average of  
310 the 13:30 and 01:30 LW calculations, it doesn't matter which time we use). The magnitude of  
311 the diurnal approximation uncertainty is very variable for different cloud types. The SW diurnal  
312 approximation uncertainty is smallest (less than  $0.25 \text{ W m}^{-2}$ ) for the contribution of HxMxL to the  
313 regional mean *CRE*. The SW diurnal approximation uncertainty is largest (almost  $7 \text{ W m}^{-2}$ ) for the  
314 contribution of 1L to the regional mean *CRE*. The SW diurnal approximation uncertainty for 1L  
315 is large due to large changes in its frequency at 01:30 compared to 13:30 (c.f. Fig. 4). The diurnal  
316 mean approximation uncertainty in the LW is smaller; the largest LW uncertainty is approximately  
317  $2.5 \text{ W m}^{-2}$  for the contribution of HL to the TOA *CRE*.

318 To account for uncertainty related to our radiative transfer calculations, we produce a second  
319 estimate of the *CRE*, where we use the comparison with CERES described in section 2b to exclude  
320 CCCM group profiles corresponding to large TOA irradiance errors, as explained below. This is  
321 referred to as “the constrained dataset” hereafter. Using the constrained dataset, a second estimate  
322 of the *CCRE* is calculated for each cloud type. The difference between the *CCRE* from the full  
323 dataset and the constrained dataset is used as an estimate of uncertainty. However, we have no  
324 direct evidence that the cloud type frequencies are incorrect (or a justifiable alternative estimate of

325 the cloud type frequencies), so we do not use the constrained dataset to calculate the frequency of  
326 occurrence of the cloud types. Thus  $CRE^k$  for each cloud type,  $k$ , from the constrained dataset is  
327 calculated as the product of the  $CCRE^k$  from the constrained dataset and  $F^k$  from the full dataset.

328 In order to exclude CCCM group profiles with large errors, we need to determine error thresholds  
329 for both the SW and LW calculations. Moreover, we do not want to exclude CCCM group profiles  
330 where the difference between the calculated irradiance and CERES measurements may be due  
331 to the representativeness differences between CERES and CloudSat-CALIPSO. As a result, we  
332 determine these thresholds based on the mean spatial variability between CERES measurements.  
333 We first calculate mean absolute differences in the irradiance for adjacent CERES pixels along the  
334 CloudSat-CALIPSO flight track. The thresholds are set as the 90th percentile of these differences,  
335 with independent thresholds for the SW and LW.

336 The resulting error thresholds in SW and LW are  $132.6 \text{ W m}^{-2}$  and  $28.3 \text{ W m}^{-2}$ , respectively. The  
337 difference between our calculations and the corresponding CERES measurements exceeds one of  
338 these thresholds for approximately 32.4 % of CERES footprints during the day and 21.6 % at night.  
339 Unsurprisingly, once we exclude these points, the remaining points have improved correlations  
340 with CERES observations increasing from 0.92 to 0.95 for the OSR, from 0.85 to 0.97 for the  
341 daytime OLR, and from 0.91 to 0.97 for the nighttime OLR. The OLR biases are reduced both for  
342 day and night from  $-20.5$  to  $-8.9 \text{ W m}^{-2}$  and from  $-1.1$  to  $-0.2 \text{ W m}^{-2}$ , respectively. However, the  
343 magnitude of the OSR bias increases from  $-4.7$  to  $-12.4 \text{ W m}^{-2}$ . The majority (approximately 56  
344 %) of the daytime points that are excluded from this refined dataset are 1H and HL cloud types.  
345 This is consistent with the low-cloud misattribution hypothesis, because these are the cloud types  
346 for which the extinction from any missing low-cloud will be attributed to high cloud and thus have  
347 a particularly large effect on the OLR. Generally, the magnitude of the calculation uncertainty is

348 quite small (less than  $1.5 \text{ W m}^{-2}$ ), with the exceptions being the calculation uncertainty for the  
349 contribution of 1H ( $\sim 2 \text{ W m}^{-2}$ ) and HL ( $\sim 6 \text{ W m}^{-2}$ ) to the 13:30 LW TOA *CRE*.

350 As highlighted previously, these three sources of uncertainty are calculated independently and  
351 combined in quadrature. For the instantaneous irradiances, we only have sampling and calculation  
352 uncertainty and the calculation uncertainty is generally the larger of the two. For diurnal mean  
353 irradiances, the SW uncertainty due to sampling and the calculations is much smaller than the  
354 instantaneous uncertainty at 13:30, because the diurnal mean SW irradiances are much smaller  
355 than the 13:30 values. For both SW and LW diurnal mean irradiances, the dominant source of  
356 uncertainty depends on the cloud type. The largest combined (SW+LW) uncertainty is for 1L due  
357 to SW diurnal approximation uncertainty, and HL due to calculation uncertainty in the LW.

### 358 **3. The radiative effects of different cloud types**

359 The frequency of occurrence of the different cloud types is shown in Fig. 4. Cloud frequency of  
360 occurrence at 13:30 and 01:30 are calculated and shown separately. SWA is very cloudy, and has  
361 infrequent clear sky (less than 10 %), in agreement with existing cloud climatologies (e.g., Hill  
362 et al. 2016). The most common cloud types are 1L, 1H, and HL, but eight of the twelve cloud types  
363 occur at least 5% of the time in this region, indicating a much more diverse set of cloud types than  
364 those found in many other parts of the globe (e.g., Tselioudis et al. 2013; Bodas-Salcedo et al.  
365 2016). Multi-layer clouds (i.e. where distinct clouds occur simultaneously in multiple layers)  
366 occur frequently (42 % during the day and 46 % during the night), representing a further source of  
367 complexity for understanding cloud radiative effects.

368 Isolated low-cloud (1L) is one of the most common cloud types with a daytime frequency of  
369 17 % and a nighttime frequency of 7 %. Low-cloud occurs even more frequently beneath other  
370 cloud layers; the combined isolated and discontiguous low-cloud frequencies are 48 % and 36 %

371 for daytime and nighttime, respectively. Including contiguous low-cloud increases frequencies to  
372 67 % during the day and 56 % at night, consistent with the value of 60 % reported in Knippertz  
373 et al. (2011) based on surface observations at Kumasi. The CCCM product may also miss some  
374 low-cloud beneath high cloud, as explained in the previous section.

375 The increase in high cloud at night is in agreement with previous analyses of cloud cover in this  
376 region from both CloudSat-CALIPSO and MODIS (e.g., Stein et al. 2011; Hill et al. 2016), as is  
377 the increase in low-cloud cover during the day. However, the Kumasi observations in Knippertz  
378 et al. (2011) show similar low-cloud cover at 01:30 and 13:30 local time. The domain mean  
379 increase in low-cloud cover in the CCCM dataset during the day is driven by a larger daytime  
380 increase in low-cloud cover to the north of the domain as previously detailed by van der Linden  
381 et al. (2015). Including only CCCM data between 6 °N and 7 °N (Kumasi is at 6.7 °N), gives  
382 smaller day-night differences with total discontinuous low-cloud cover of 50 % during the day,  
383 and 47 % at night.

384 Figure 5a shows that the mean SW TOA coincident cloud radiative effect (*CCRE*) of each cloud  
385 type is strongly linked to the number of layers it extends through, which is an indication of the  
386 cloud physical thickness. Physical thickness is in turn correlated with water path and optical depth  
387 (Wang et al. 2000). The HxMxL cloud type, which extends into three layers and is likely to be  
388 deep convection, has the largest mean SW *CCRE* (476 W m<sup>-2</sup> at 13:30). Those cloud types that  
389 extend between two layers have the next largest mean SW *CCRE* with values ranging from 275 –  
390 297 W m<sup>-2</sup> at 13:30. Clouds that occur separately in one or more layers have 13:30 values ranging  
391 from 150 to 187 W m<sup>-2</sup>.

392 The diurnal mean downwelling SW irradiance at TOA is approximately 36 % of the mean value  
393 for the 13:30 overpasses (not shown). However, for upwelling SW radiation at the TOA, the SW  
394 diurnal approximation (indicated by the dashed lines on the bars in Fig. 5a) gives *CCRE* values

395 between 36 % and 40 % as large as the instantaneous 13:30 calculations, depending on cloud type.  
396 These ratios differ between cloud types because of the increased atmospheric path length as the  
397 solar zenith angle increases. This leads to an increase in the extinction of the direct solar beam  
398 due to cloud, which has a bigger impact on the SW *CCRE* of clouds that are less optically thick.  
399 Consequently, for the diurnal mean, the relative difference between *CCRE*s for different cloud  
400 types is less than for the 13:30 calculations.

401 The TOA LW *CCRE*, shown in Fig. 5b, is of a smaller magnitude than the diurnal mean TOA  
402 SW *CCRE* for almost all cloud types, with isolated high cloud being the exception. As expected  
403 the magnitude of LW TOA *CCRE* is determined by cloud top temperature, and thus closely linked  
404 to the presence of high cloud.

405 For all cloud types, the LW TOA *CCRE* is larger during the day than at night. Since TOA  
406 downwelling LW irradiances are zero, the LW TOA *CCRE* is calculated by subtracting the all-  
407 sky OLR from the clear-sky OLR. As a result, the LW TOA *CCRE* can be increased by either  
408 increasing the clear-sky OLR or decreasing the all-sky OLR. In the SOCRATES calculations, both  
409 these effects occur. A warmer surface temperature during the day leads to a larger value for the  
410 clear-sky OLR. Larger ice mass mixing ratios during the day lead to smaller values for the all-sky  
411 OLR. The daytime increase in the LW TOA *CCRE* for isolated low-clouds is driven by the increase  
412 in the clear-sky OLR. The daytime increase in the LW TOA *CCRE* for high clouds is driven  
413 by larger daytime ice mass mixing ratios. Note that the daytime all-sky OLR is underestimated  
414 compared to CERES (Fig 2b). Moreover, these larger daytime ice mass mixing ratios may not be  
415 realistic, and are consistent with the low-cloud misattribution hypothesis.

416 Using the constrained dataset (i.e. excluding CCCM group profiles where there is a large dis-  
417 crepancy between the calculated and observed irradiances in either the SW or LW), Fig. 5 shows  
418 that the exclusion has a relatively small effect on the mean daytime SW or nighttime LW *CCRE*,

419 but has a larger effect on the mean LW daytime *CCRE*. The biggest effect is for the HL cloud  
420 type, where the mean *CCRE* reduces in magnitude from 61 to 31  $\text{W m}^{-2}$ . The H, HM, HML, and  
421 HML cloud types also have a reduction in magnitude of the mean daytime LW *CCRE* of 10–20  
422  $\text{W m}^{-2}$ . Errors in these cloud types suggest high clouds are too optically thick, which is consistent  
423 with the low-cloud misattribution hypothesis. Intriguingly the day-night differences in the mean  
424 LW *CCRE* at TOA are reduced, compared to the full dataset. This provides further evidence that  
425 the diurnal differences found in the mean TOA LW *CCRE* in the full dataset may be artificial, due  
426 to errors in cloud properties.

427 Figure 6 shows the contribution to the regional mean SW *CRE* at TOA, at the surface, and within  
428 the atmosphere from each cloud type. The regional mean *CRE* is simply the sum of the *CRE* values  
429 for each cloud type. At the TOA, three cloud types stand out: vertically deep cloud (HxMxL), high  
430 cloud above low-cloud (HL), and isolated low-cloud (1L). HxMxL has the largest SW *CRE* due to  
431 its large mean *CCRE* as shown in Fig. 5a. In contrast, 1L and HL have large SW *CRE* due to their  
432 relatively high frequency of occurrence as shown in Fig. 4. However, we emphasize that these  
433 three cloud types together account for only approximately 50 % of the regional mean SW *CRE* at  
434 the TOA; the other cloud types have non-negligible radiative effects. Indeed, explaining 75 % of  
435 the regional mean SW *CRE* requires 6 cloud types, and explaining 90 % requires 9 of the 12 cloud  
436 types.

437 The contribution of the 12 different cloud types to the surface *CRE* (Fig. 6b) is similar to the  
438 TOA both in total magnitude and relative contribution of the different cloud types (Fig. 6a). This  
439 is because SW atmospheric absorption is small and most of the SW extinction is due to scattering.

440 As SW atmospheric absorption is small, the surface and TOA *CRE*s are of a similar magnitude,  
441 and the in-atmosphere *CRE* is small. The small in-atmosphere *CRE* that does occur (Fig. 6c) is  
442 due to a combination of increased atmospheric path length for radiation reflected by low-cloud and

443 absorption of near-infrared radiation by cloud. With an in-cloud *CRE* of approximately  $5 \text{ W m}^{-2}$ ,  
444 HxMxL, HL and 1L once again have the largest *CRE*s.

445 Compared to the SW *CRE*, the LW *CRE* shows more complex behavior. For the TOA (Fig.  
446 7a), since the LW *CCRE* largely depends on the cloud top temperature (as shown in Fig. 5b), the  
447 standout cloud types become HxMxL and HL, and 1H. In contrast to the SW TOA *CRE*, isolated  
448 low-cloud (1L), has a rather small impact on the LW *CRE* at the TOA, as it has a small *CCRE*  
449 (Fig. 5b). The three dominant cloud types account for approximately 60 % of the regional mean  
450 LW *CRE* at the TOA, so as in the SW, other cloud types make a non-negligible contribution to the  
451 regional mean *CRE*.

452 At the surface, the LW *CCRE* is strongly dependent on cloud base height. Consequently, the  
453 contributions of the different cloud types to the regional mean LW *CRE* are quite different to those  
454 for the LW *CRE* at the TOA. The three dominant cloud types for the LW *CRE* at the surface are 1L,  
455 HL, and HxMxL. Coincidentally, these match the three dominant cloud types in the SW. As for  
456 the SW *CRE* at all heights, and the LW *CRE* at the TOA, other cloud types make non-negligible  
457 contributions to the regional mean LW *CRE* at the surface.

458 As the TOA and surface LW *CRE*s are quite different, the in-atmosphere *CRE*s show a large  
459 range between cloud types. In the presence of isolated low-clouds, the net LW irradiance increases  
460 at the surface and decrease at the TOA. Since the magnitude of the former is greater than the latter,  
461 isolated low-clouds cause LW cooling of the atmosphere, as shown in Fig. 7c. For high top clouds,  
462 the decrease in *CRE* at the TOA is larger in magnitude than the increase in *CRE* at the surface, so  
463 high cloud cause LW heating of the atmosphere. Adding low-cloud beneath high cloud leads to a  
464 larger magnitude LW irradiance increase at the surface, so that the LW heating of the atmosphere  
465 is less than it would be in the absence of the low-clouds (e.g. during the day, HL occurs more  
466 frequently than 1H and has a larger *CRE* at the TOA, but a smaller effect on the in-atmosphere

467 *CRE*). Mid-level top clouds lead to cooling above the cloud, and heating beneath the cloud; this  
468 affects the vertical temperature gradient of the atmosphere, but has little effect on the vertically  
469 integrated atmospheric heating.

470 At the TOA and surface, the difference between calculations for day and night are generally less  
471 than  $5 \text{ W m}^{-2}$ , and of varying sign depending on cloud type (larger surface LW *CRE* in the day for  
472 1L but smaller TOA LW *CRE* in the day for 1H). These day-night differences are primarily due to  
473 the contrasting frequencies of occurrence between day and night (Fig. 4), except for the HL cloud  
474 type, where the day-night differences are primarily due to differences in the *CCRE* (Fig. 5).

475 Uncertainty in LW contributions to the *CRE* are estimated from the constrained dataset (star  
476 symbols). The low-cloud misattribution hypothesis posits that the CCCM dataset overestimates  
477 extinction by high-cloud due to missing low-cloud. However, we have no objective estimate of  
478 how this missing low-cloud will affect the frequencies of the different cloud types. Consequently,  
479 we use the original cloud type frequencies to calculate *CRE* contributions in the constrained  
480 dataset; only the mean *CCRE* is changed. As a result, TOA differences between the full and  
481 constrained datasets follows the pattern described for the mean *CCRE*. At the surface the differ-  
482 ences are much smaller. However the constrained dataset results in a larger contribution from HL  
483 during the day to the surface LW *CRE*. This results in a difference of  $6 \text{ W m}^{-2}$  between the two  
484 calculations for flux into the atmosphere.

485 Figure 8 shows the approximate diurnal mean total (i.e. SW + LW) cloud radiative effects. This  
486 is the sum of the SW and LW diurnal mean approximations. The error bars show the combined  
487 uncertainty due to the SW and LW diurnal mean approximations, differences between the full and  
488 refined datasets, and sampling errors. These three sources of uncertainty are estimated separately  
489 for the SW and LW, resulting in a total of 6 values that are combined by summing in quadrature.

490 The diurnal mean total irradiances tend to be small due to cancellation between LW and SW  
491 *CREs*. For some cloud types, uncertainty is quite large (up to  $\pm 7 \text{ W m}^{-2}$ ) at the TOA and surface,  
492 but the uncertainty is generally much smaller for fluxes into the atmosphere. At the TOA, the 1L  
493 cloud type has the largest magnitude net *CRE*, as the decrease in net downwelling SW TOA irra-  
494 diance due to low-clouds is much larger than the increase in net downwelling LW TOA irradiance.  
495 Most other cloud types also have a negative effect on the TOA net downwelling irradiance, though  
496 for many cloud types this is not certain. Isolated high cloud (1H) is the only cloud type that defi-  
497 nitely leads to an increase in the net TOA irradiance. All cloud types reduce the net downwelling  
498 irradiance at the surface, due to the reduction in SW radiation reaching the surface being larger  
499 than the increase in downwelling LW radiation. 1L leads to a small reduction in the flux into the  
500 atmosphere, but all other cloud types increase the flux into the atmosphere.

#### 501 **4. Sensitivity of radiative fluxes to low-cloud cover errors**

502 As noted in the introduction and our analysis of the CCCM cloud types, low-cloud is common  
503 in SWA. Yet low-cloud cover is generally underestimated in climate models, which is thought to  
504 be responsible for large surface SW radiation biases in these models (e.g., Knippertz et al. 2011;  
505 Hannak et al. 2017). In this section we assess the potential role of low altitude cloud cover errors  
506 in contributing to radiation budget biases through sensitivity studies. To this end, we estimate ir-  
507 radiance sensitivity to low-cloud cover errors by comparing the existing SOCRATES calculations  
508 with further calculations that mimic the low-cloud bias in models by removing cloud water content  
509 beneath 680 hPa. The bias due to removing all low-clouds, which we denote  $\Delta CRE_{low}$  is calcu-  
510 lated by subtracting the *CRE* based on the original calculations from the *CRE* based on the new  
511 calculations where low-cloud is removed. Like the *CRE*, this can be separated into contributions  
512 from the different cloud types  $\Delta CRE_{low}^k$ .

513 Figure 9 shows the cumulative change in approximate diurnal mean irradiances from  $\Delta CRE_{-low}^k$   
514 for all cloud types that include low-cloud. Note that for ease of comparison to the Hannak et al.  
515 (2017) study, we show downwelling surface irradiances rather than net (down-up) downwelling  
516 surface irradiance as in all other figures. First,  $\Delta CRE_{-low}^k$  shows large variation between cloud  
517 types. The irradiances are most sensitive to changes in low-cloud cover for 1L, while the irra-  
518 diances are least sensitive to changes in low-cloud cover for HxMxL. This is because  $\Delta CRE_{-low}^k$   
519 strongly depends on the presence of other cloud in the profile. For example, for the 1L cloud  
520 type, removing the low-cloud results in clear-sky, so much more SW radiation reaches the surface.  
521 On the contrary, for HxMxL, removing the low-cloud has a much smaller impact on the down-  
522 welling surface SW radiation, as the remaining cloud above 680 hPa reflects a large amount of  
523 SW radiation (9d).

524 So that Fig. 9 can be used to estimate the likely irradiance error for a given low-cloud cover  
525 error, the change in both low-cloud cover and irradiances associated with each cloud type are  
526 plotted cumulatively. Clearly, as  $\Delta CRE_{-low}^k$  depends on cloud type, there is a range of possible  
527 irradiances for a given low-cloud cover error. To capture this, we plot the cumulative irradiance  
528 error in order of both increasing and decreasing magnitude of  $\Delta CRE_{-low}^k$  per unit change in low-  
529 cloud cover, which correspond to the minimum and maximum irradiance error for a given change  
530 in low-cloud cover respectively. The relative importance of low-cloud to different cloud types  
531 is similar for both SW and LW irradiances at both TOA and the surface. However, the relative  
532 importance of low-cloud to HL compared to other cloud types for the downwelling surface LW  
533 irradiance is larger than for the the SW and surface LW irradiances, due to high cloud having little  
534 effect on the downwelling LW irradiance at the surface.

535 The net (SW+LW) error due to low-cloud cover errors may be as large as  $24 \text{ W m}^{-2}$  for the  
536 downwelling surface irradiance and  $23 \text{ W m}^{-2}$  for the outgoing irradiance at the TOA. Errors of

537 this magnitude in an atmospheric model are likely to impact on the regional circulation and pre-  
538 cipitation. For example, Li et al. (2015) linked radiative perturbations of a similar magnitude to  
539 monthly mean precipitation changes of up to 60 mm month<sup>-1</sup> in simulations of the WAM.

540 Coming back to the issue with large surface SW radiation biases found in models, Knippertz  
541 et al. (2011) showed a multi-model mean bias of approximately 30 W m<sup>-2</sup> in downwelling surface  
542 SW irradiances over SWA during June-September using CMIP3 (Coupled Model Intercomparison  
543 Project phase 3) simulations. A similar analysis of YOTC (Year of Tropical Convection) simu-  
544 lations revealed a multi-model mean bias of  $\sim 25$  W m<sup>-2</sup>. Based on Fig. 9d, the CMIP3 bias is  
545 equivalent to a low-cloud cover error of between  $-0.48$  and  $-0.61$ , as illustrated by the thin broken  
546 grey lines. Similarly, the YOTC bias (not shown) is equivalent to a low-cloud cover error of be-  
547 tween  $-0.37$  and  $-0.55$ . Since such large low-cloud cover biases are required to produce the SW  
548 irradiance biases seen in models, we conclude that models must also underestimate the occurrence  
549 of other cloud types in this region.

550 In summary, low-cloud cover errors are expected to lead to large errors in diurnal mean SW  
551 irradiances; up to 35 W m<sup>-2</sup> for the downwelling surface irradiance and up to 25 W m<sup>-2</sup> for the  
552 OSR. These are offset somewhat by smaller changes in LW irradiances of up to 11 W m<sup>-2</sup> at  
553 the surface and 2 W m<sup>-2</sup> at the TOA. Errors of this magnitude are sufficient to affect the WAM  
554 circulation in atmospheric models. However, the 30 W m<sup>-2</sup> mean bias in the downwelling surface  
555 SW irradiance simulated by CMIP3 climate models is unlikely to be solely due to low-cloud errors.

## 556 **5. Summary**

557 Southern West Africa (SWA) is a region where clouds are poorly understood, and the large-scale  
558 circulation is sensitive to radiative perturbations. To better understand cloud-radiation interactions  
559 in this region, we have classified clouds into 12 distinct types based on vertical structure, and

560 quantified the radiative effect of these cloud types at the surface, TOA, and on heating/cooling of  
561 the atmosphere. We have focused in particular on low-clouds, which are poorly understood since  
562 they are often obscured in satellite imagery and there is currently a lack of surface observations in  
563 the region.

564 SWA experiences many different cloud types; no single cloud type dominates in terms of either  
565 frequency of occurrence, or radiative effect. The most frequent cloud types are 1L, 1H, HL, and  
566 HxMxL, (See Fig. 3 for definitions) which have frequencies of 12, 14, 19, and 10 %, respectively.  
567 Contributions from different cloud types to the regional mean cloud radiative effect depend not  
568 only on their frequencies, but also on their mean coincident radiative effects (*CCRE*), which are  
569 linked to cloud thickness in the SW, and cloud top and base height in the LW.

570 The regional energy budget links cloud radiative effects to precipitation and circulation (e.g. Hill  
571 et al. 2016). As a summary of the contribution of different cloud types to the regional diurnal mean  
572 energy budget, Fig. 10 shows how the net effect on atmospheric heating for each cloud type can be  
573 explained by contrasting SW and LW effects at the surface and TOA. Uncertainty is denoted by the  
574  $\pm$  values, rounded to the nearest integer, and shows the combined uncertainty due to uncertainty in  
575 the diurnal mean approximation, differences between the full and refined datasets, and sampling  
576 errors. In order to reduce the number of panels, we show the four most frequent cloud types  
577 independently and divide the remaining cloud types into two categories, mid-level top and high  
578 top. All cloud types lead to a net cooling of the surface, ranging from approximately  $2 \text{ W m}^{-2}$  for  
579 ML to  $13 \text{ W m}^{-2}$  for HxMxL. 1H results in an increase in the net downwelling irradiance at the  
580 TOA ( $4 \text{ W m}^{-2}$ ), but all other cloud types have the opposite effect. 1L leads to small cloud radiative  
581 cooling of the atmosphere, but all other cloud types lead to heating.

582 Uncertainty in the cloud radiative effects remains due to the limited diurnal sampling and dif-  
583 ferences between the calculations and CERES measurements. The frequency of low-clouds may

584 also be underestimated in the CCCM data product. Our calculations have been evaluated by com-  
585 parison of the TOA irradiances with coincident CERES measurements. We find good agreement  
586 for SW and nighttime LW irradiances, but our calculations underestimate the OLR during the day-  
587 time. This is thought to be due to problems identifying low-cloud from satellites, which may lead  
588 to the misattribution of low-cloud extinction to higher clouds in the CCCM dataset.

589 Focusing on low-cloud, we have shown that it occurs much more frequently below other clouds  
590 (30 %) than by itself (12 %). As a result, passive satellites, which are unable to detect low-cloud  
591 beneath other clouds, will miss much of the low-cloud in SWA. Isolated low-cloud (1L) is the  
592 only cloud type that contributes a net cooling to the atmosphere. This is due to LW cooling of  
593 the atmosphere, which predominantly occurs within the cloud, and is due to an increase in the  
594 downwelling LW irradiance. This is offset by relatively large (compared to the other cloud types)  
595 SW heating of the atmosphere, due to gaseous absorption of the increased upwelling SW radiation  
596 that is reflected by the cloud.

597 Discontiguous low-cloud plays a less obvious role in reducing cloud radiative heating of the  
598 atmosphere. When low-cloud co-occurs with higher cloud, the radiative heating of the atmosphere  
599 due to the higher cloud tends to be larger than the cooling effect of the low-cloud. However, the  
600 radiative heating of the atmosphere is less than it would be in the absence of the low-cloud. For  
601 example, Fig. 10 shows cloud radiative heating of the atmosphere is less for HL than for 1H, even  
602 though HL occurs more often (19 % compared to 14 %). Further calculations where low-cloud is  
603 removed as described in the previous section show that the presence of low-cloud in HL reduces  
604 the cloud radiative heating of the atmosphere by  $2 \text{ W m}^{-2}$ . The presence of low-cloud also reduces  
605 the cloud radiative heating of the atmosphere for the other cloud types where discontiguous low-  
606 cloud is present (i.e. ML, HML, and HxML in addition to HL). The total cloud radiative heating  
607 of the atmosphere is  $37 \text{ W m}^{-2}$ ; with the cooling from low-cloud being approximately  $-4 \text{ W m}^{-2}$ .

608 Sensitivity to underestimating low-cloud cover was examined by comparing calculations with  
609 and without low-cloud; underestimating low-cloud cover led to a downwelling SW irradiance  
610 error of up to  $33 \text{ W m}^{-2}$ , and an OSR error of up to  $24 \text{ W m}^{-2}$ . Thus low-cloud errors are unlikely  
611 to be solely responsible for the  $25\text{--}30 \text{ W m}^{-2}$  multi-model mean surface downwelling SW errors  
612 in SWA identified in climate models (Knippertz et al. 2011; Hannak et al. 2017). However, the  
613 effect of underestimating low-cloud is undoubtedly significant. Errors of a similar magnitude have  
614 been linked to large changes in monsoon circulation and monsoon precipitation in regional climate  
615 simulations (Li et al. 2015).

616 We anticipate that these calculations will provide a useful tool for evaluating cloud radiation  
617 interactions in this region in atmospheric models, and the method can be extended to other regions,  
618 or even globally. This will require model diagnostics that assign cloud types to model columns in  
619 the same manner as this study. Many climate models already include the COSP simulator package  
620 (Bodas-Salcedo et al. 2011), which could be used to diagnose the frequency of different cloud  
621 profiles within the model and thereby generate the diagnostics required. Such diagnostics would  
622 provide a useful tool for evaluating the cloud in models. We see two key advantages to this method  
623 for evaluating models. Firstly, separating different cloud types will help to reveal compensating  
624 errors between different cloud types and similarly, separating frequency of occurrence and *CCRE*  
625 for each cloud type will reveal compensating error for individual cloud types, such as the “too few  
626 too bright” problem in climate models (Nam and Quaas 2012). Secondly, as the formation and  
627 dissipation of different cloud types are linked to different physical processes, attributing model  
628 errors to different cloud types will aid identification of problematic cloud processes in the model.

629 Cloud and radiation measurements taken during the DACCIWA field campaign (Flamant et al.  
630 2017) provide a complementary dataset to the calculations described here, with better identifi-  
631 cation of low-cloud and diurnal sampling, but a limited time period (June-July 2016) and worse

632 spatial sampling. The DACCIWA project is also working with weather services in SWA, to extend  
633 the availability of existing surface measurements, and provide further cloud data. Future work will  
634 exploit these surface-based datasets alongside satellite observations to refine our understanding of  
635 low-cloud and its influence on the regional energy budget.

636 *Acknowledgments.* The research leading to this publication has received funding from the Eu-  
637 ropean Union 7th Framework Programme (FP7/2007-2013) under grant agreement 603502 (EU  
638 project DACCIWA: Dynamics-Aerosol-Chemistry-Cloud Interactions in West Africa). A. B-S was  
639 supported by the Joint UK BEIS/Defra Met Office Hadley Centre Climate Programme (GA01101).  
640 CCCM data were obtained from the NASA Langley Research Center Atmospheric Sciences Data  
641 Center (<http://eosweb.larc.nasa.gov>). GERB data can be accessed via ftp from the Royal Meteoro-  
642 logical Institute of Belgium (<ftp://gerb.oma.be>).

## 643 **References**

- 644 Adler, B., N. Kalthoff, and L. Gantner, 2017: Nocturnal low-level clouds over southern West  
645 Africa analysed using high-resolution simulations. *Atmospheric Chemistry and Physics*, **17** (2),  
646 899–910.
- 647 Baran, A. J., P. Field, K. Furtado, J. Manners, and A. Smith, 2013: A new high- and low-frequency  
648 scattering parameterization for cirrus and its impact on a high-resolution numerical weather  
649 prediction model. *AIP Conf. Proc.*, **1531**, 716–719.
- 650 Baran, A. J., P. Hill, D. Walters, S. C. Hardiman, K. Furtado, P. R. Field, and J. Manners, 2016: The  
651 Impact of Two Coupled Cirrus Microphysics–Radiation Parameterizations on the Temperature  
652 and Specific Humidity Biases in the Tropical Tropopause Layer in a Climate Model. *Journal of*  
653 *Climate*, **29** (14), 5299–5316.

- 654 Birch, C. E., J. H. Marsham, D. J. Parker, and C. M. Taylor, 2014: The scale dependence and  
655 structure of convergence fields preceding the initiation of deep convection. *Geophysical Re-*  
656 *search Letters*, **41 (13)**, 4769–4776.
- 657 Bodas-Salcedo, A., P. G. Hill, K. Furtado, K. D. Williams, P. R. Field, J. C. Manners, P. Hyder,  
658 and S. Kato, 2016: Large Contribution of Supercooled Liquid Clouds to the Solar Radiation  
659 Budget of the Southern Ocean. *Journal of Climate*, **29 (11)**, 4213–4228.
- 660 Bodas-Salcedo, A., and Coauthors, 2011: COSP: Satellite simulation software for model assess-  
661 ment. *Bull. Amer. Meteor. Soc.*, **92 (8)**, 1023–1043.
- 662 Bouniol, D., F. Couvreux, P.-H. Kamsu-Tamo, M. Leplay, F. Guichard, F. Favot, and E. J.  
663 O’Connor, 2012: Diurnal and Seasonal Cycles of Cloud Occurrences, Types, and Radiative  
664 Impact over West Africa. *J. Appl. Meteor. Climatol.*, **51 (3)**, 534–553.
- 665 Collow, A. B., V. P. Ghate, M. A. Miller, and L. C. Trabachino, 2015: A one-year study of the  
666 diurnal cycle of meteorology, clouds and radiation in the West African Sahel region. *Quarterly*  
667 *Journal of the Royal Meteorological Society*, **142 (694)**, 16–29.
- 668 Cook, K. H., and E. K. Vizzy, 2006: Coupled Model Simulations of the West African Monsoon  
669 System: Twentieth- and Twenty-First-Century Simulations. *J. Climate*, **19 (15)**, 3681–3703.
- 670 Cusack, S., A. Slingo, J. M. Edwards, and M. Wild, 1998: The radiative impact of a simple  
671 aerosol climatology on the Hadley Centre atmospheric GCM. *Quarterly Journal of the Royal*  
672 *Meteorological Society*, **124 (551)**, 2517–2526.
- 673 Dewitte, S., L. Gonzalez, N. Clerbaux, A. Ipe, C. Bertrand, and B. D. Paepe, 2008: The Geo-  
674 stationary Earth Radiation Budget Edition 1 data processing algorithms. *Advances in Space*  
675 *Research*, **41 (11)**, 1906–1913.

- 676 Edwards, J. M., and A. Slingo, 1996: Studies with a flexible new radiation code. 1: Choosing a  
677 configuration for a large-scale model. *Q. J. Roy. Meteorol. Soc.*, **122**, 690–719.
- 678 Flamant, C., and Coauthors, 2017: The Dynamics-Aerosol-Chemistry-Cloud Interactions in West  
679 Africa field campaign: Overview and research highlights. *Bull. Amer. Meteor. Soc.*, **In press**.
- 680 Futyan, J. M., J. E. Russel, and J. E. Harries, 2005: Determining cloud forcing by cloud type from  
681 geostationary satellite data. *Geophys. Res. Lett.*, **32 (8)**, –.
- 682 Ham, S.-H., and Coauthors, 2017: Cloud occurrences and cloud radiative effects (CREs) from  
683 CERES-CALIPSO-CloudSat-MODIS (CCCM) and CloudSat radar-lidar (RL) products. *Journal of Geophysical Research: Atmospheres*, **122 (16)**, 8852–8884.
- 684
- 685 Hannak, L., P. Knippertz, A. H. Fink, A. Kniffka, and G. Pante, 2017: Why Do Global Climate  
686 Models Struggle to Represent Low-Level Clouds in the West African Summer Monsoon? *Journal of Climate*, **30 (5)**, 1665–1687.
- 687
- 688 Harries, J. E., and Coauthors, 2005: The Geostationary Earth Radiation Budget Project. *Bull.*  
689 *Amer. Meteor. Soc.*, **86 (7)**, 945–960.
- 690 Hartmann, D. L., M. E. Ockert-Bell, and M. L. Michelsen, 1992: The Effect of Cloud Type on  
691 Earth's Energy Balance: Global Analysis. *Journal of Climate*, **5 (11)**, 1281–1304.
- 692 Hill, P. G., R. P. Allan, J. C. Chiu, and T. H. M. Stein, 2016: A multi-satellite climatology of  
693 clouds, radiation and precipitation in southern West Africa and comparison to climate models.  
694 *Journal of Geophysical Research: Atmospheres*, –.
- 695 Hong, Y., G. Liu, and J.-L. F. Li, 2016: Assessing the Radiative Effects of Global Ice Clouds  
696 Based on CloudSat and CALIPSO Measurements. *Journal of Climate*, **29 (21)**, 7651–7674.

- 697 Hourdin, F., and Coauthors, 2010: AMMA-Model Intercomparison Project. *Bulletin of the Amer-*  
698 *ican Meteorological Society*, **91** (1), 95–104.
- 699 Kato, S., 2003: Computation of domain-averaged shortwave irradiance by a one-dimensional al-  
700 gorithm incorporating correlations between optical thickness and direct incident radiation. *J.*  
701 *Atm. Sci.*, **60** (1), 182–193.
- 702 Kato, S., S. Sun-Mack, W. F. Miller, F. G. Rose, Y. Chen, P. Minnis, and B. A. Wielicki, 2010:  
703 Relationships among cloud occurrence frequency, overlap and effective thickness derived from  
704 CALIPSO and CloudSat merged vertical profiles. *J. Geophys. Res.*, **115** (D00H28).
- 705 Kato, S., and Coauthors, 2011: Improvements of top-of-atmosphere and surface irradiance compu-  
706 tations with CALIPSO-, CloudSat-, and MODIS-derived cloud and aerosol properties. *Journal*  
707 *of Geophysical Research*, **116** (D19), –.
- 708 Knippertz, P., M. J. Evans, P. R. Field, A. H. Fink, C. Lioussé, and J. H. Marsham, 2015a: The  
709 possible role of local air pollution in climate change in West Africa. *Nature Climate Change*,  
710 **5** (9), 815–822.
- 711 Knippertz, P., A. H. Fink, R. Schuster, J. Trentmann, J. M. Schrage, and C. Yorke, 2011: Ultra-low  
712 clouds over the southern West African monsoon region. *Geophys. Res. Lett.*, **38** (21), n/a–n/a.
- 713 Knippertz, P., and Coauthors, 2015b: The DACCIWA Project: Dynam-  
714 ics–Aerosol–Chemistry–Cloud Interactions in West Africa. *Bull. Amer. Meteor. Soc.*, **96** (9),  
715 1451–1460.
- 716 Li, R., J. Jin, S.-Y. Wang, and R. R. Gillies, 2015: Significant impacts of radiation physics in the  
717 Weather Research and Forecasting model on the precipitation and dynamics of the West African  
718 Monsoon. *Clim Dyn*, **44** (5-6), 1583–1594.

719 Mace, G. G., Q. Zhang, M. Vaughan, R. Marchand, G. Stephens, C. Trepte, and D. Winker, 2009:  
720 A description of hydrometeor layer occurrence statistics derived from the first year of merged  
721 CloudSat and CALIPSO data. *J. Geophys. Res.*, **114** (D00A26).

722 Marsham, J. H., N. S. Dixon, L. Garcia-Carreras, G. M. S. Lister, D. J. Parker, P. Knippertz, and  
723 C. E. Birch, 2013: The role of moist convection in the West African monsoon system: Insights  
724 from continental-scale convection-permitting simulations. *Geophys. Res. Lett.*, **40** (9), 1843–  
725 1849.

726 Miller, M. A., V. P. Ghate, and R. K. Zahn, 2012: The Radiation Budget of the West African Sahel  
727 and Its Controls: A Perspective from Observations and Global Climate Models. *J. Climate*,  
728 **25** (17), 5976–5996.

729 Minnis, P., and Coauthors, 2011: CERES Edition-2 Cloud Property Retrievals Using TRMM  
730 VIRS and Terra and Aqua MODIS Data — Part I: Algorithms. *IEEE Trans. Geosci. Remote*  
731 *Sensing*, **49** (11), 4374–4400.

732 Nam, C., S. Bony, J.-L. Dufresne, and H. Chepfer, 2012: The ‘too few, too bright’ tropical low-  
733 cloud problem in CMIP5 models. *Geophys. Res. Lett.*, **39** (21), n/a–n/a.

734 Nam, C. C. W., and J. Quaas, 2012: Evaluation of clouds and precipitation in the ECHAM5 general  
735 circulation model using CALIPSO and CloudSat satellite data. *J. Climate*, **25** (14), 4975–4992.

736 Nicholson, S. E., and J. P. Grist, 2003: The Seasonal Evolution of the Atmospheric Circulation  
737 over West Africa and Equatorial Africa. *Journal of Climate*, **16** (7), 1013–1030.

738 Oreopoulos, L., N. Cho, and D. Lee, 2017: New insights about cloud vertical structure from Cloud-  
739 Sat and CALIPSO observations. *Journal of Geophysical Research: Atmospheres*, **122** (17),  
740 9280–9300.

741 Paeth, H., and Coauthors, 2011: Progress in regional downscaling of west African precipitation.  
742 *Atmosph. Sci. Lett.*, **12** (1), 75–82.

743 Rodwell, M. J., and T. Jung, 2008: Understanding the local and global impacts of model physics  
744 changes: an aerosol example. *Quarterly Journal of the Royal Meteorological Society*, **134** (635),  
745 1479–1497.

746 Roehrig, R., D. Bouniol, F. Guichard, F. Hourdin, and J.-L. Redelsperger, 2013: The Present and  
747 Future of the West African Monsoon: A Process-Oriented Assessment of CMIP5 Simulations  
748 along the AMMA Transect. *J. Climate*, **26** (17), 6471–6505.

749 Schrage, J. M., S. Augustyn, and A. H. Fink, 2006: Nocturnal stratiform cloudiness during the  
750 West African monsoon. *Meteorol. Atmos. Phys.*, **95** (1-2), 73–86.

751 Schuster, R., A. H. Fink, and P. Knippertz, 2013: Formation and Maintenance of Nocturnal Low-  
752 Level Stratus over the Southern West African Monsoon Region during AMMA 2006. *Journal*  
753 *of the Atmospheric Sciences*, **70** (8), 2337–2355.

754 Stein, T. H. M., D. J. Parker, J. Delano, N. S. Dixon, R. J. Hogan, P. Knippertz, R. I. Maidment,  
755 and J. H. Marsham, 2011: The vertical cloud structure of the West African monsoon: A 4 year  
756 climatology using CloudSat and CALIPSO. *J. Geophys. Res.*, **116** (D22), n/a–n/a.

757 Stein, T. H. M., D. J. Parker, R. J. Hogan, C. E. Birch, C. E. Holloway, G. M. S. Lister, J. H.  
758 Marsham, and S. J. Woolnough, 2015: The representation of the West African monsoon vertical  
759 cloud structure in the Met Office Unified Model: an evaluation with CloudSat. *Q.J.R. Meteorol.*  
760 *Soc.*, n/a–n/a.

- 761 Taylor, J. P., J. M. Edwards, M. D. Glew, P. Hignett, and A. Slingo, 1996: Studies with a flexible  
762 new radiation code. II: Comparisons with aircraft short-wave observations. *Quarterly Journal*  
763 *of the Royal Meteorological Society*, **122 (532)**, 839–861.
- 764 Tompkins, A. M., 2005: Influence of aerosol climatology on forecasts of the African Easterly Jet.  
765 *Geophysical Research Letters*, **32 (10)**, –.
- 766 Tselioudis, G., W. Rossow, Y. Zhang, and D. Konsta, 2013: Global Weather States and Their  
767 Properties from Passive and Active Satellite Cloud Retrievals. *Journal of Climate*, **26 (19)**,  
768 7734–7746.
- 769 van der Linden, R., A. H. Fink, and R. Redl, 2015: Satellite-based climatology of low-level conti-  
770 nental clouds in southern West Africa during the summer monsoon season. *Journal of Geophys-*  
771 *ical Research: Atmospheres*, **120 (3)**, 1186–1201.
- 772 Wang, J., W. B. Rossow, and Y. Zhang, 2000: Cloud vertical structure and its variations from a  
773 20-yr global rawinsonde dataset. *Journal of Climate*, **13 (17)**, 3041–3056.

774 **LIST OF FIGURES**

775 **Fig. 1.** Schematic illustrating how measurements from different instruments are combined to form  
776 CCCM group profiles (also known as cloud groups) in the CCCM dataset. Based on Kato  
777 et al. (2011). . . . . 37

778 **Fig. 2.** Comparison of SOCRATES-calculated shortwave (SW) and longwave (LW) outgoing irra-  
779 diances at the top of the atmosphere with co-located CERES observations that are taken  
780 from the integrated CCCM product. SOCRATES values are weighted means of the calcu-  
781 lations for each CCCM cloud group within the corresponding CERES footprint, where the  
782 weighting is determined by the fraction of the CERES footprint occupied by each cloud  
783 group. Shading represents joint frequency of occurrence. Correlation coefficient and bias  
784 ( $W m^{-2}$ ) with respect to CERES observations are listed in each subplot. . . . . 38

785 **Fig. 3.** Illustrative schematic of the twelve cloud types used in this study. L, M, and H are used to  
786 respectively denote low-, mid-, and high-level clouds, separated using pressure levels of 680  
787 and 440 hPa. Symbol x indicates that two layers are contiguous in the vertical extent. . . . . 39

788 **Fig. 4.** June-September 2006-2010 mean frequency of occurrence of each cloud type in the CCCM  
789 product over SWA. Cloud frequency of occurrence at 13:30 and 01:30 are normalized sep-  
790 arately. Uncertainty due to sampling is illustrated by the error bars, which show the 95%  
791 confidence interval based on bootstrapping. . . . . 40

792 **Fig. 5.** June-September 2006-2010 SOCRATES calculated mean SW (top) and LW (bottom) mean  
793 coincident cloud radiative effect (*CCRE*) at the TOA over SWA. Bars labeled 01:30 and  
794 13:30 correspond to calculations based on the nighttime and daytime satellite overpasses,  
795 respectively. The diurnal approximation shown in SW (top) plot is based on averaging calcu-  
796 lations that use the daytime CCCM data and a range of solar zenith angles, as explained  
797 in section 2c. Uncertainty due to errors in our calculations is illustrated by the constrained  
798 calculations, which exclude CCCM group profiles where the SOCRATES-CERES TOA dif-  
799 ferences are large, as explained in section 2e. Error bars show the 95% confidence interval  
800 based on bootstrapping. . . . . 41

801 **Fig. 6.** Contribution to the regional mean SW *CRE* from each cloud type for June-September, 2006-  
802 2010 over SWA at (a) TOA, (b) surface and (c) in-atmosphere, based on SOCRATES cal-  
803 culations. The 13:30 calculations, use the 13:30 CCCM data with the corresponding solar  
804 zenith angle. The SW diurnal approximation is based on averaging calculations that use the  
805 13:30 CCCM data and a range of solar zenith angles, as explained in section 2c. Uncer-  
806 tainty due to errors in our calculations is illustrated by the constrained calculations, which  
807 exclude CCCM group profiles where the SOCRATES-CERES TOA differences are large, as  
808 explained in section 2e. Error bars show the 95% confidence interval based on bootstrapping. . . . . 42

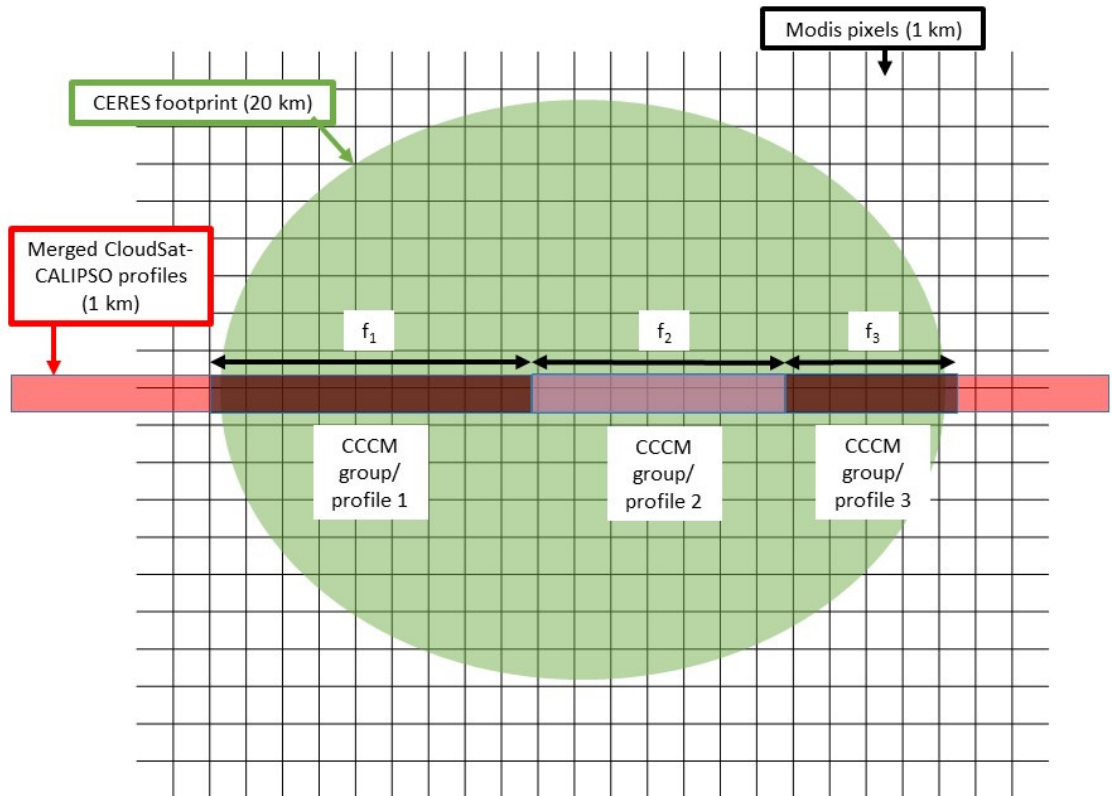
809 **Fig. 7.** As Fig. 6, but for LW. . . . . 43

810 **Fig. 8.** Contribution to the diurnal mean total (i.e. SW + LW) *CRE* from each cloud type for June-  
811 September 2006-2010 over SWA, based on SOCRATES calculations. Error bars show the  
812 combined uncertainty due to the diurnal mean approximation, the constrained calculation  
813 (which exclude CCCM group profiles where the SOCRATES-CERES TOA differences are  
814 large, as explained in section 2e) and the limited sampling. These uncertainties are calcu-  
815 lated separately for the SW and LW, and are combined in quadrature. . . . . 44

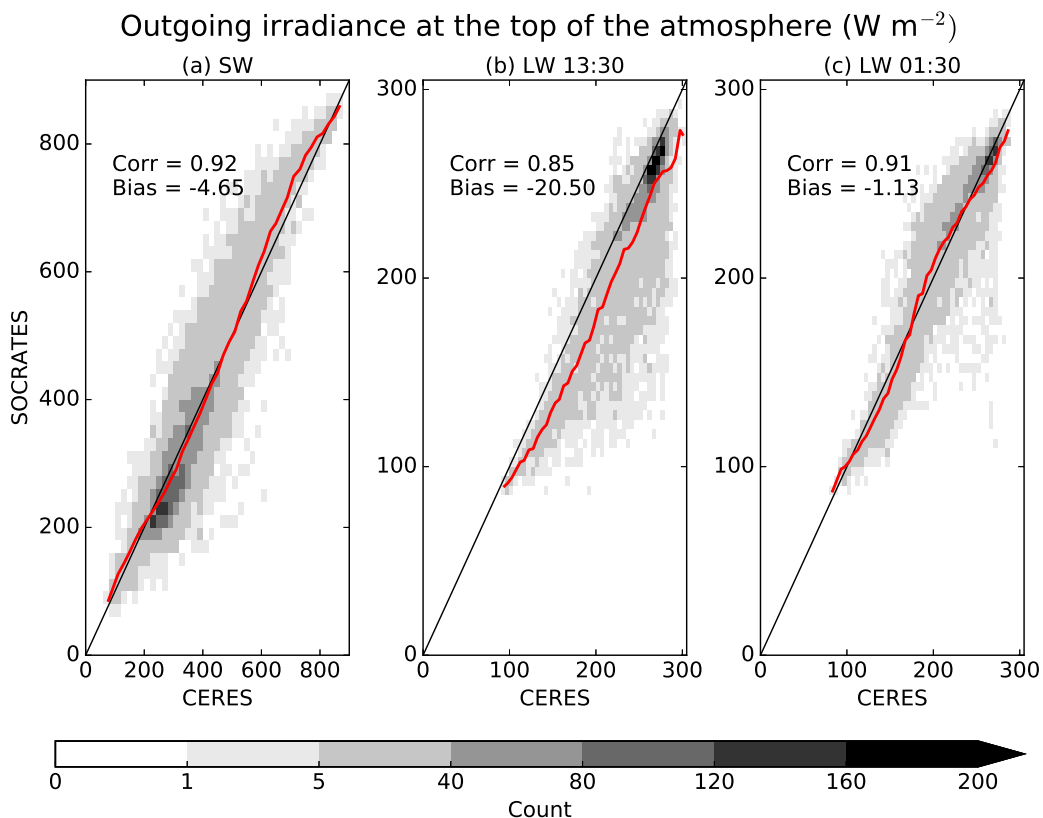
816 **Fig. 9.** Cumulative change in diurnal mean irradiance due to removing low-cloud for different cloud  
817 types for June-September 2006-2010. Calculated as the difference between the original cal-

818 calculations and further calculations where all cloud water content beneath 680 hPa is removed.  
 819 Each labeled line shows the change in low-cloud cover (horizontal extent of the line) and  
 820 irradiance (vertical extent of the line) caused by removing low-cloud for the cloud type indi-  
 821 cated on the label. The cloud types are plotted according to the magnitude of the change in  
 822 irradiance per unit change in cloud cover. Both increasing and decreasing order are plotted,  
 823 which show the lower and upper bounds for the irradiance change for a given change in low-  
 824 cloud cover, respectively. The grey dash-dot lines show the range of low-cloud cover errors  
 825 required to produce the modeled irradiance bias of  $30 \text{ W m}^{-2}$  identified by Knippertz et al.  
 826 (2011). The low-cloud cover increments (x-axis) for each cloud type match the frequency of  
 827 occurrence shown in Fig. 4 As we show changes in diurnal mean irradiance, the SW values  
 828 are based on cloud cover at 13:30 and the LW values are based on the average of the 01:30  
 829 and 13:30 low-cloud cover. . . . . 45

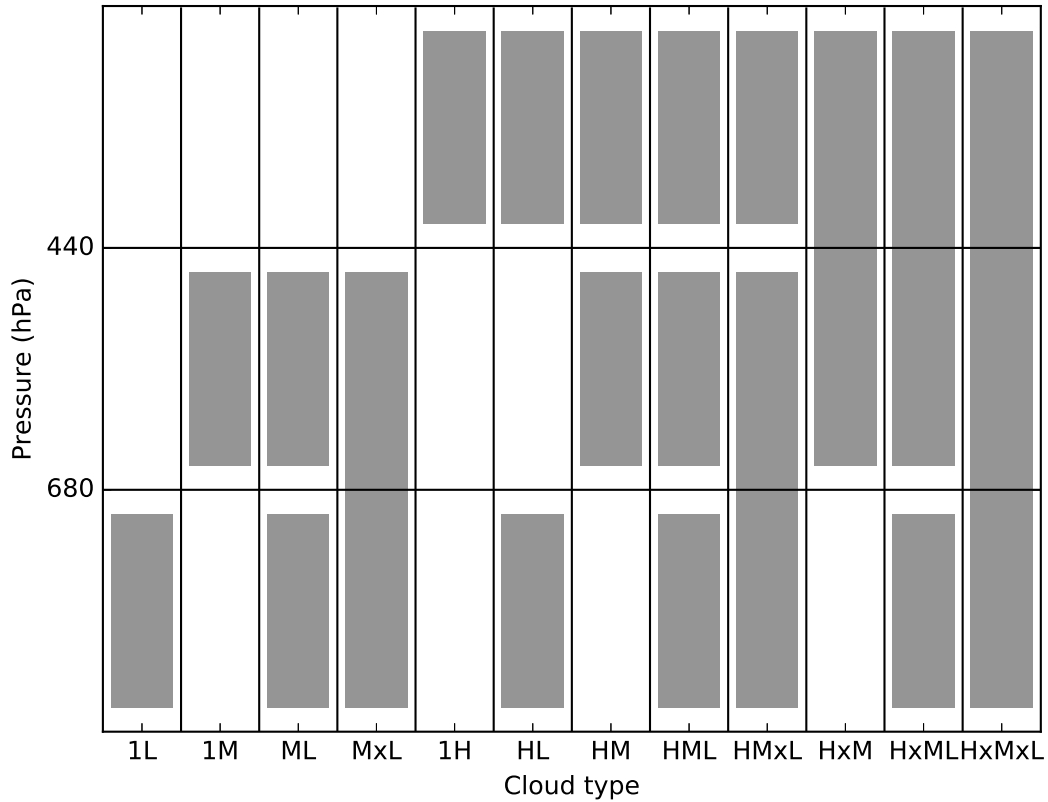
830 **Fig. 10.** Schematic illustrating the contribution of different cloud types to the diurnal mean radiation  
 831 budget of the atmosphere of SWA for June-September 2006-2010. The direction each arrows  
 832 point in indicates the direction of the *CRE* for that cloud type and the area of each arrow is  
 833 proportional to the magnitude of the *CRE*. The  $\pm$  values indicate uncertainty, as explained  
 834 in the text. To reduce the number of panels in the schematic, we show the four most frequent  
 835 cloud types (1L, 1H, HL and HxMxL) and the remaining cloud types are split into mid-level  
 836 top and high-top and the combined radiative effects are shown. Note that all values are  
 837 rounded to the nearest integer. . . . . 46



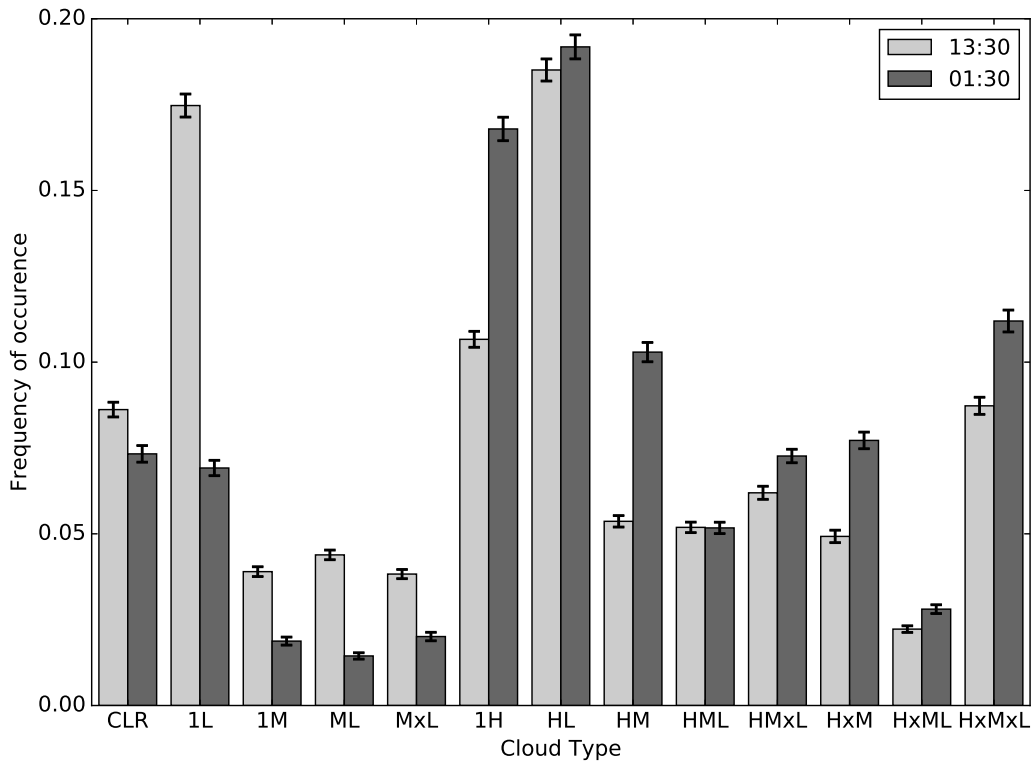
838 FIG. 1. Schematic illustrating how measurements from different instruments are combined to form CCCM  
 839 group profiles (also known as cloud groups) in the CCCM dataset. Based on Kato et al. (2011).



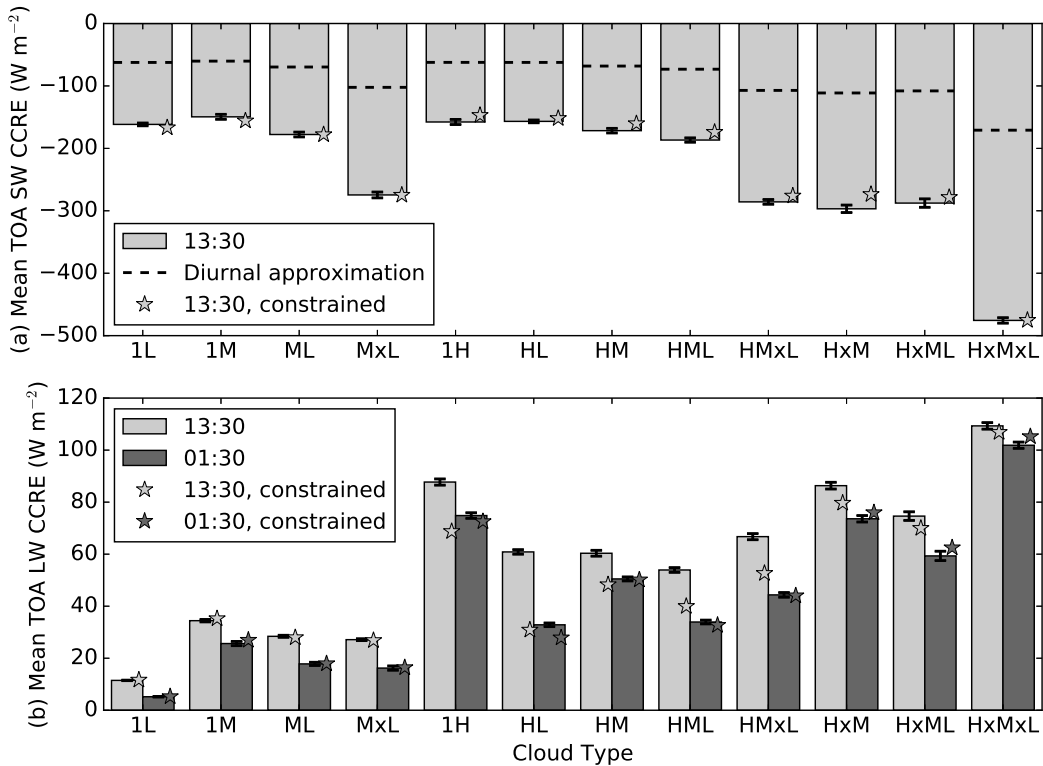
840 FIG. 2. Comparison of SOCRATES-calculated shortwave (SW) and longwave (LW) outgoing irradiances  
 841 at the top of the atmosphere with co-located CERES observations that are taken from the integrated CCCM  
 842 product. SOCRATES values are weighted means of the calculations for each CCCM cloud group within the  
 843 corresponding CERES footprint, where the weighting is determined by the fraction of the CERES footprint  
 844 occupied by each cloud group. Shading represents joint frequency of occurrence. Correlation coefficient and  
 845 bias ( $\text{W m}^{-2}$ ) with respect to CERES observations are listed in each subplot.



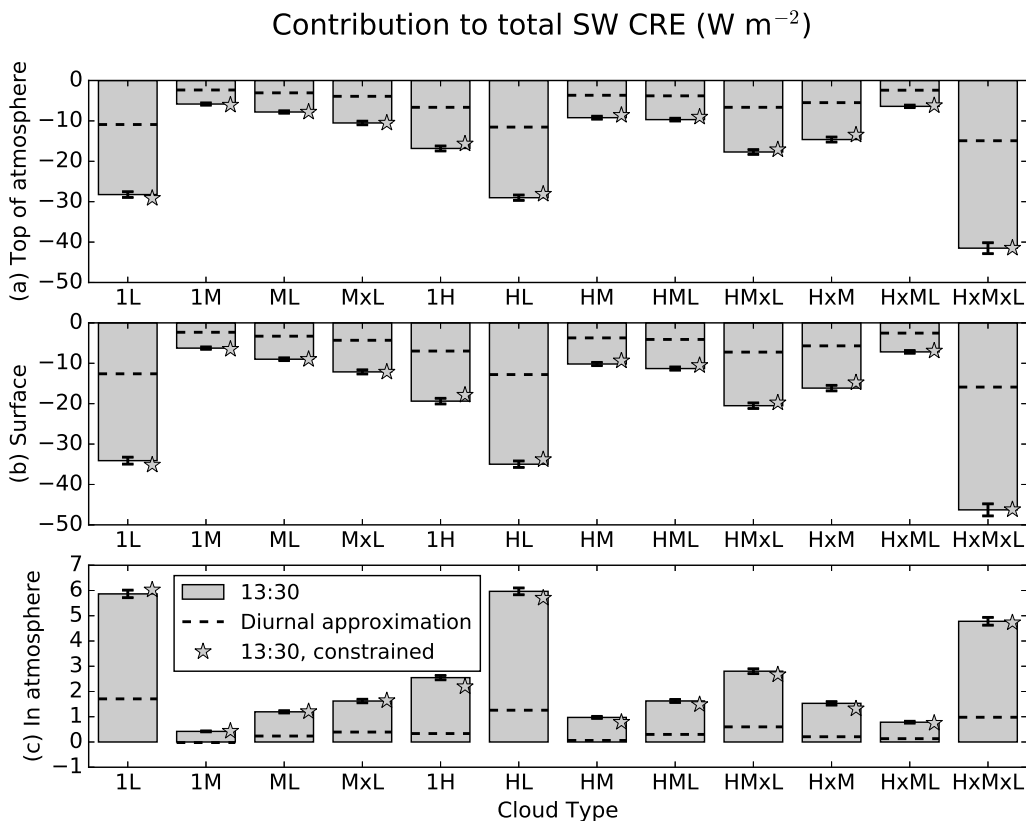
846 FIG. 3. Illustrative schematic of the twelve cloud types used in this study. L, M, and H are used to respectively  
 847 denote low-, mid-, and high-level clouds, separated using pressure levels of 680 and 440 hPa. Symbol x indicates  
 848 that two layers are contiguous in the vertical extent.



849 FIG. 4. June-September 2006-2010 mean frequency of occurrence of each cloud type in the CCCM product  
 850 over SWA. Cloud frequency of occurrence at 13:30 and 01:30 are normalized separately. Uncertainty due to  
 851 sampling is illustrated by the error bars, which show the 95% confidence interval based on bootstrapping.



852 FIG. 5. June-September 2006-2010 SOCRATES calculated mean SW (top) and LW (bottom) mean coincident  
 853 cloud radiative effect (CCRE) at the TOA over SWA. Bars labeled 01:30 and 13:30 correspond to calculations  
 854 based on the nighttime and daytime satellite overpasses, respectively. The diurnal approximation shown in  
 855 SW (top) plot is based on averaging calculations that use the daytime CCCM data and a range of solar zenith  
 856 angles, as explained in section 2c. Uncertainty due to errors in our calculations is illustrated by the constrained  
 857 calculations, which exclude CCCM group profiles where the SOCRATES-CERES TOA differences are large, as  
 858 explained in section 2e. Error bars show the 95% confidence interval based on bootstrapping.



859 FIG. 6. Contribution to the regional mean SW CRE from each cloud type for June-September, 2006-2010 over  
 860 SWA at (a) TOA, (b) surface and (c) in-atmosphere, based on SOCRATES calculations. The 13:30 calculations,  
 861 use the 13:30 CCCM data with the corresponding solar zenith angle. The SW diurnal approximation is based on  
 862 averaging calculations that use the 13:30 CCCM data and a range of solar zenith angles, as explained in section  
 863 2c. Uncertainty due to errors in our calculations is illustrated by the constrained calculations, which exclude  
 864 CCCM group profiles where the SOCRATES-CERES TOA differences are large, as explained in section 2e.  
 865 Error bars show the 95% confidence interval based on bootstrapping.

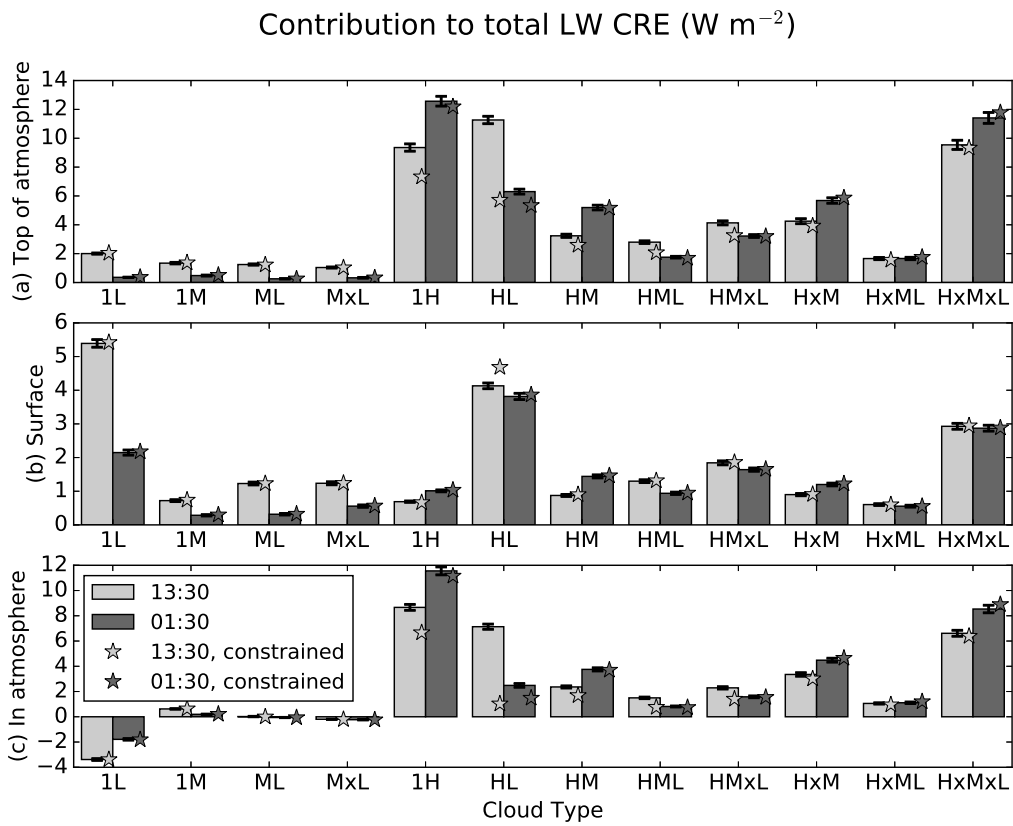
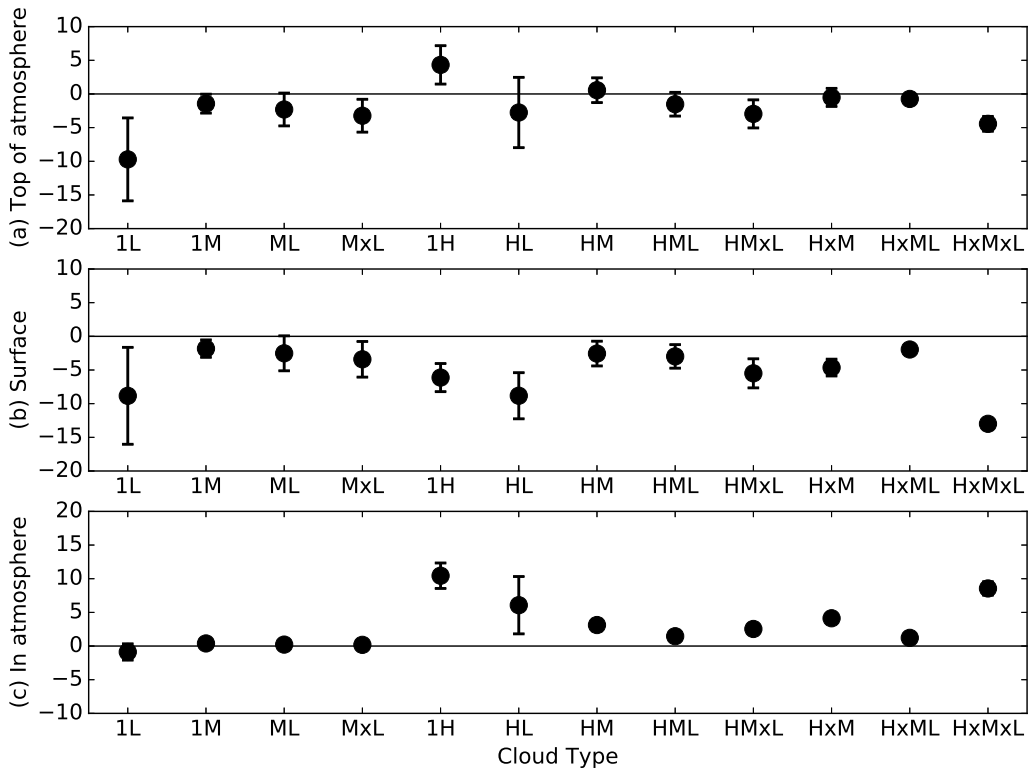
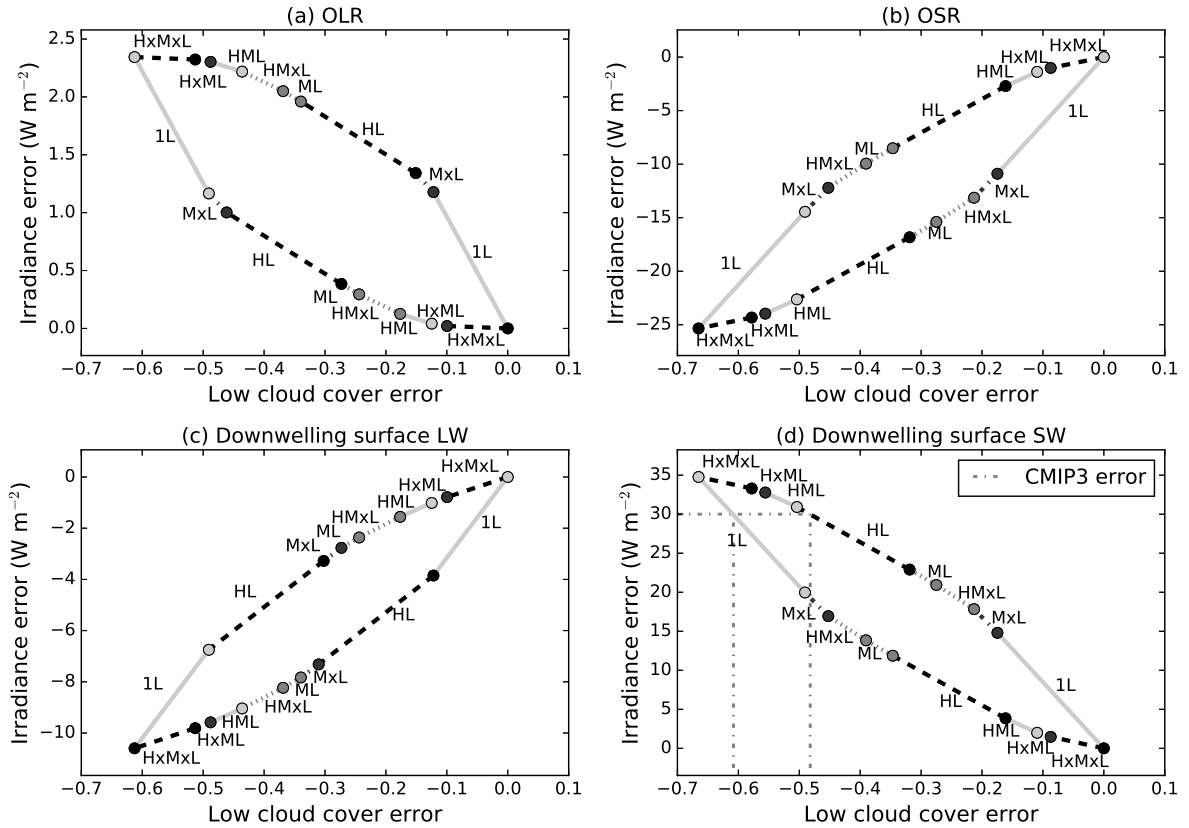


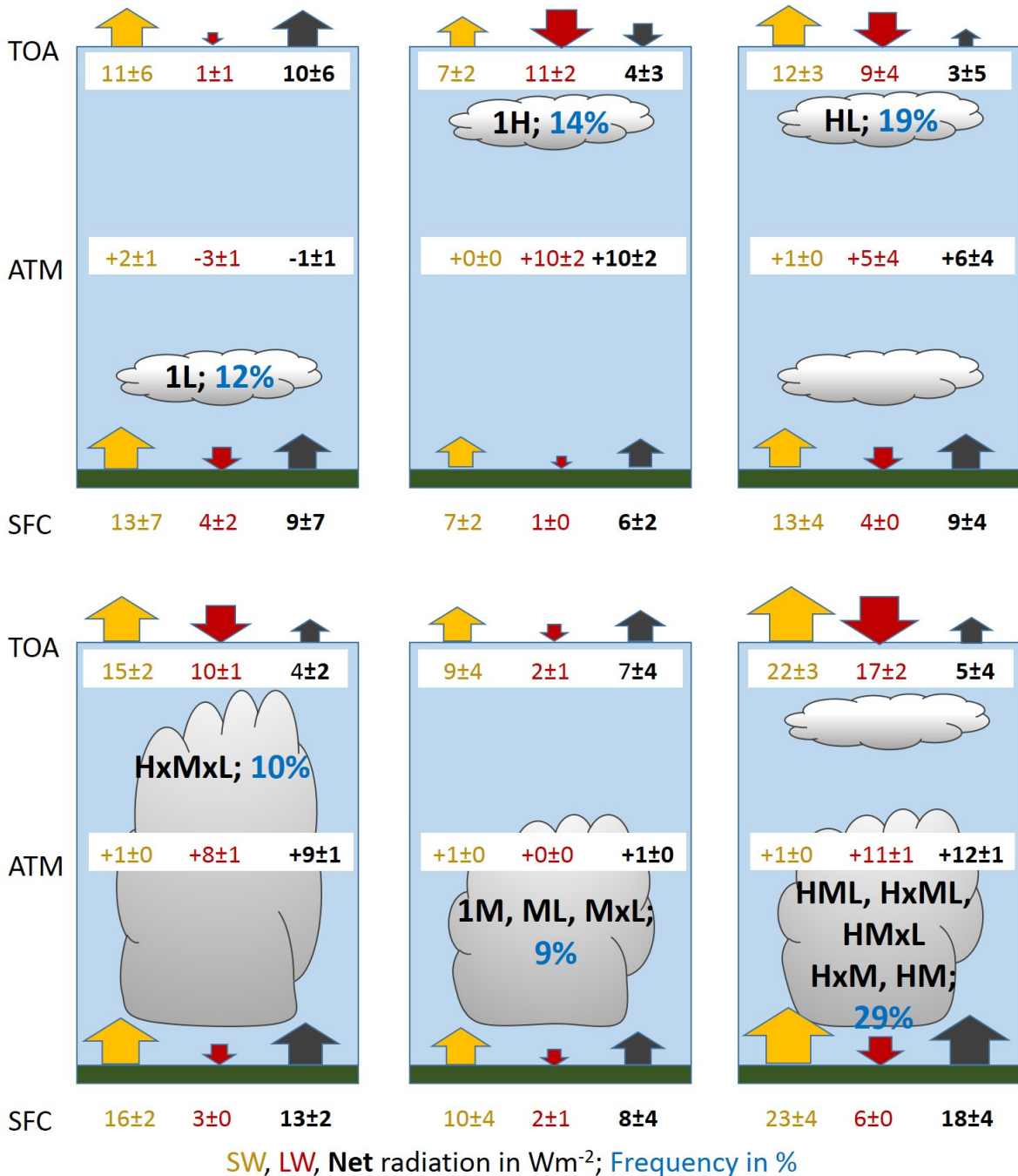
FIG. 7. As Fig. 6, but for LW.



866 FIG. 8. Contribution to the diurnal mean total (i.e. SW + LW) CRE from each cloud type for June-September  
 867 2006-2010 over SWA, based on SOCRATES calculations. Error bars show the combined uncertainty due to  
 868 the diurnal mean approximation, the constrained calculation (which exclude CCCM group profiles where the  
 869 SOCRATES-CERES TOA differences are large, as explained in section 2e) and the limited sampling. These  
 870 uncertainties are calculated separately for the SW and LW, and are combined in quadrature.



871 FIG. 9. Cumulative change in diurnal mean irradiance due to removing low-cloud for different cloud types  
 872 for June-September 2006-2010. Calculated as the difference between the original calculations and further cal-  
 873 culations where all cloud water content beneath 680 hPa is removed. Each labeled line shows the change in  
 874 low-cloud cover (horizontal extent of the line) and irradiance (vertical extent of the line) caused by removing  
 875 low-cloud for the cloud type indicated on the label. The cloud types are plotted according to the magnitude of  
 876 the change in irradiance per unit change in cloud cover. Both increasing and decreasing order are plotted, which  
 877 show the lower and upper bounds for the irradiance change for a given change in low-cloud cover, respectively.  
 878 The grey dash-dot lines show the range of low-cloud cover errors required to produce the modeled irradiance  
 879 bias of  $30 \text{ W m}^{-2}$  identified by Knippertz et al. (2011). The low-cloud cover increments (x-axis) for each cloud  
 880 type match the frequency of occurrence shown in Fig. 4 As we show changes in diurnal mean irradiance, the  
 881 SW values are based on cloud cover at 13:30 and the LW values are based on the average of the 01:30 and 13:30  
 882 low-cloud cover.



883 FIG. 10. Schematic illustrating the contribution of different cloud types to the diurnal mean radiation budget  
 884 of the atmosphere of SWA for June-September 2006-2010. The direction each arrows point in indicates the  
 885 direction of the *CRE* for that cloud type and the area of each arrow is proportional to the magnitude of the *CRE*.  
 886 The  $\pm$  values indicate uncertainty, as explained in the text. To reduce the number of panels in the schematic, we  
 887 show the four most frequent cloud types (1L, 1H, HL and HxMxL) and the remaining cloud types are split into  
 888 mid-level top and high-top and the combined radiative effects are shown. Note that all values are rounded to the  
 889 nearest integer.